

The nature of inclusions in glendonites from the Paleocene Basilika Formation on Svalbard

David Rijkes

1st examiner: Bas van de Schootbrugge

2nd examiner: Helen King

Department of Earth Sciences, Utrecht University, Utrecht, Netherlands.

21 March 2022

Abstract

Glendonites are authigenic carbonate minerals formed after diagenetic transformation of the metastable hydrated carbonate mineral ikaite ($\text{CaCO}_3 \cdot 6\text{H}_2\text{O}$). Since ikaite is only stable at low temperatures, glendonites are being used as proxies for cold climate conditions. Paradoxically, glendonites have been found in hothouse periods, such as the Eocene, Paleocene, Cretaceous, and Jurassic. In addition to low temperatures, other conditions are likely also important in driving ikaite precipitation and glendonite transformation, including elevated concentrations of P and Mg, and sulphate reduction coupled to methane oxidation. Here, we further examine the processes leading to ikaite transformation based on combined microscopic and organic geochemical analyses of glendonites from a drill core spanning the Paleocene Basilika Formation on Svalbard. Thin section analyses showed multiple growth generations of calcium carbonate in the glendonites, referred to as Type 1a, Type 1b, and Type 2. Biomarker analyses showed a strong presence of oil in both glendonites and surrounding sediments. Fluid inclusions mainly characterise carbonate generations Type 1a and 1b and can be shown to contain droplets of oil. Raman spectroscopy showed the principal calcium carbonate phase of glendonites to be calcite. In this work the presence of inclusions containing oil is used to evaluate ikaite-glendonite transformation mechanisms. Two new transformation mechanisms are proposed for the formation of the inclusion-rich type 1 generations. One mechanism involves calcium carbonate crystal nucleation on oil-water interfaces, the other involves interface-coupled dissolution-precipitation of ikaite to glendonite. Further research is warranted to determine the role of fluid inclusions in widespread ikaite formation.

Introduction

Glendonites are formed from the diagenesis of the metastable carbonate mineral ikaite ($\text{CaCO}_3 \cdot 6\text{H}_2\text{O}$) (Suess et al., 1982; Swainson & Hammond, 2001). Ikaite can transform into the pseudomorph glendonite when temperatures reach above 5 to 15 degrees Celsius in the natural environment (Pauly, 1963; Bischoff et al., 1993; Larsen, 1994; Stockmann et al., 2018), but can also remain stable until higher temperatures when the pressure is higher (Marland, 1975). While low temperature conditions are favourable for ikaite crystallization, glendonites have been found in periods thought to have been hothouses, such as the Eocene (e.g. Qu et al., 2017), Paleocene (e.g. den Boer, 2019), Cretaceous (e.g. Morales et al., 2017; Vickers et al., 2018; den Boer, 2019), and Jurassic (e.g. Teichert & Luppold, 2013; Morales et al., 2017). This hints that additional processes effect ikaite formation. Seawater is normally undersaturated with respect to ikaite, but increases in saturation with lower temperatures (Bischoff et al., 1993). Once supersaturated, ikaite precipitation is favoured when other forms of calcium carbonate such as calcite and aragonite are inhibited. An

increase in phosphate and magnesium concentration can serve as inhibiting effects on calcite and aragonite crystallization (Bischoff et al., 1993). Sulphate acts as an inhibitor for calcite and high-Mg calcite and will favour aragonite precipitation (Savard et al., 1996). However, when seawater is supersaturated with respect to ikaite, an increase in sulphate will lead to an increase in ikaite precipitation (Bischoff et al., 1993). Increasing the pH also favours ikaite precipitation (Tollefsen et al., 2018). When the geochemical conditions in the water change from favouring ikaite deposition to favouring the deposition of other forms of calcium carbonate ikaite can transform into glendonite (Greinert & Derkachev, 2004). During the transformation, ikaite loses the water in its crystal structure, which makes up 68.6% of the total volume (Shearman & Smith, 1985). Synthetic ikaite is shown to have a euhedral texture, sometimes with cavities, while synthetic glendonite is shown to be porous with a fibrous texture, sometimes with large cavities (Tollefsen et al., 2020). While many studies successfully recreated ikaite in the laboratory at specific conditions (e.g. Bischoff et al., 1993; Tang et al., 2009; Sánchez-Pastor et al., 2016; Tollefsen et al., 2020), little is known about how ikaite is formed in the natural environment. Furthermore, the transformation mechanism from ikaite to glendonite in the natural environment is also still unresolved.

Previous work analysed the $\delta^{13}\text{C}$ signal of bulk glendonites to identify the carbon source of the glendonites in order to investigate the environmental conditions in which these, and its precursor, were formed (Greinert & Derkachev, 2004; Selleck et al., 2007; Spielhagen & Tripathi, 2009; Teichert & Luppold, 2013; Morales et al., 2017; Vickers et al., 2018; Vickers et al., 2020). These authors found values ranging from -45‰ to 0‰, encompassing the biogenic and thermogenic regime of methane $\delta^{13}\text{C}$ and even the area of (an)aerobic oxidation of organic matter (Whiticar, 1999). Since there is almost no fractionation between ikaite and glendonite (Greinert & Derkachev, 2004), the $\delta^{13}\text{C}$ of glendonites will be similar to that of ikaite. Ikaite is thought to have only a minor fractionation upon crystallization from water (about 5‰, Lu et al., 2012), so the carbon source of ikaite can be determined from $\delta^{13}\text{C}$ values of glendonites. The formation depth of marine sedimentary ikaite has been inferred to be in alkaline settings (Suess et al., 1982), and in the sulphate-methane transition zone (Zabel & Schulz, 2001; Greinert & Derkachev, 2004; Lu et al., 2012; Teichert & Luppold, 2013) using porewater Ca, DIC content, alkalinity, and $\delta^{13}\text{C}$ concentrations. They showed that Ca, DIC content, and alkalinity were all enriched during ikaite deposition. It is uncertain whether the carbon source for ikaite is solely methane or (an)aerobic oxidation of organic matter, due to the broad range found in $\delta^{13}\text{C}$ values. Many studies interpreted this broad range to reflect multiple carbon sources for ikaite (e.g. Greinert & Derkachev, 2004; Selleck et al., 2007; Teichert & Luppold, 2013; Morales et al., 2017; Qu et al., 2017; Vickers et al., 2020).

Biomarkers in glendonites have been studied (e.g. Qu et al., 2017; den Boer, 2019; Vickers et al., 2020) to identify potential microbial communities associated with ikaite formation. This information can be used to reconstruct the geochemical environment in which the ikaite was formed or was transformed into glendonite and to find out whether methane was involved in this process or not. Evidence for sulphate reduction has been found by analysis of biomarkers in glendonites (Qu et al., 2017; den Boer, 2019; Vickers et al., 2020), but evidence of anaerobic methane oxidation (AOM) is more obscure as it has only been found in biomarkers obtained from glendonites of den Boer (2019). From the polar fraction a high amount of GDGTs (Glycerol Dialkyl Glycerol Tetraethers) 1 to 3 can be related to anaerobic methane oxidation associated with methane hydrates (Pancost et al., 2001; Blumenberg et al., 2004; Pi et al., 2009). Archaeol and bacterial dialkyl glycerol diethers (DGDs) can also serve as biomarkers for AOM, however, DGDs can also have other sources (Aquilina et al., 2010). Other prominent biomarkers indicating anaerobic methane oxidation are crocetane (Elvert et al., 2000; Bian et al., 2001) and PMI (Pentamethylcosane, Aquilina et al., 2010). The hopanes 28,30-bisnorphane and 25,28,30-trisnorphane found by den Boer (2019) serve as evidence for anoxic conditions (Mello et al., 1989) and have often been found in oily sediments (Rullkötter & Wendisch,

1982; Noble et al., 1984).

To understand the process of the transformation from ikaite to glendonite various studies have looked at the petrology of marine glendonites in thin sections and have found multiple diagenetic growth generations in the structure (Larsen, 1994; Huggett et al., 2005; Teichert & Luppold, 2013; Morales et al., 2017; Vickers et al., 2018; Bloem, 2019; Vickers et al., 2020). However, there is much uncertainty regarding the origin of these generations and various models have been proposed to explain the transformation from ikaite to glendonite (e.g. Larsen, 1994; Greinert & Derkachev, 2004; Huggett et al., 2005; Teichert & Luppold, 2013; Vickers et al., 2018; Bloem, 2019; Vickers et al., 2020). Some studies have reported inclusions in some of the glendonite generations (e.g. Larsen, 1994; Huggett et al., 2005; Morales et al., 2017; Vickers et al., 2018; den Boer, 2019, Bloem, 2019), but it is poorly understood what is inside these inclusions and how they are formed. It is likely that these inclusions were formed during transformation from ikaite to glendonite as glendonites are more porous than ikaite (Tollefsen et al., 2020). Morales et al. (2017) and den Boer (2019) looked at the gas composition of these inclusions and found methane (C₁) as well as heavier hydrocarbon gases up to pentane (C₅). C₁ to C₃ hydrocarbons were also found in inclusions in methane seep carbonates (Blumenberg et al., 2018). This suggests that methane is related to glendonite transformation and/or ikaite formation. An alternative hypothesis on the transformation of ikaite to glendonite is that they are formed in the sulphate reduction zone without the involvement of methane (Qu et al., 2017; Vickers et al., 2018). Glendonites in the natural environment have largely been found in the form of calcite (e.g. Larsen, 1994; Greinert & Derkachev, 2004; Huggett et al., 2005; Selleck et al., 2007; Teichert & Luppold, 2013). However, Ito et al. (1999) also found vaterite and monohydrocalcite derived from ikaite in calcareous sediment in Shiowakka, Japan. Laboratory studies have also found that vaterite grows as an intermediate product in the transformation from ikaite to calcite (Bischoff et al., 1993; Tang et al., 2009; Sánchez-Pastor et al., 2016).

Understanding the formation of ikaite and its better preserved pseudomorph glendonite is important if those minerals serve as proxies for paleoclimate reconstructions. Stockmann et al. (2018) studied the possibility of using ikaite as mineral for carbon storage. They hypothesized that because ikaite precipitation is most favourable in colder waters, it does not require external heating to activate, which makes it profitable from an energy and resource perspective. Mangin et al. (2009) found that in a solution where all species are supersaturated precipitation of the metastable phases are generally favoured. Following this for calcium carbonate, ikaite is always metastable (Marland, 1975) and is thus favoured. Furthermore, Stockmann et al. (2018) discovered that carbon is not lost when ikaite chemically alters into glendonite. They therefore argue that ikaite can be a useful carbon sink in low temperature waters. Unfortunately, it is still uncertain what conditions are necessary for ikaite and glendonites to form. In this study Paleocene glendonites from a core of the Basilika formation in Svalbard's largest island Spitsbergen were studied for their petrology and biomarker content to gain insights in the geochemical environment in which ikaite is formed and the transformation mechanism of ikaite into glendonite.

Geological Setting

Most of the Paleocene strata in Spitsbergen are found in the Central Tertiary Basin (CTB) in the southern half of Spitsbergen (Dallmann, 1999). The CTB consists of the Van Mijenfjorden Group, which is a clastic sedimentary sequence lying unconformably on Lower Cretaceous sandstones (Dallmann, 1999). The Basilika Formation is part of the Van Mijenfjorden Group and is bound below by the Firkanten Formation and above by the Grumantbyen Formation (Fig. 1, Dallmann, 1999). The Firkanten formation is predominantly made up of marine shales and sandstones deposited in a delta

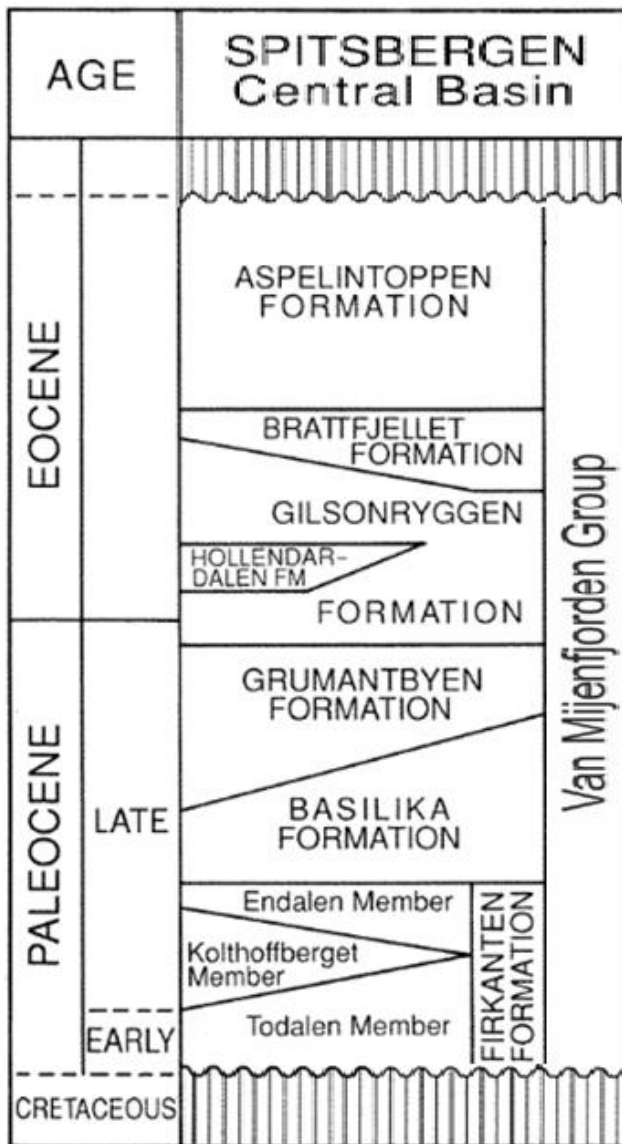


Figure 1. Stratigraphy of Paleocene deposits of the Central Basin of Spitsbergen (Modified from Nagy et al., 2000).

plain to prodelta setting (Steel et al., 1981; Muller & Spielhagen, 1990; Nagy et al., 2000). The Basilika formation consists of marine (black) shales with fossil lenses and a high abundance of pyrite (Steel et al., 1981; Müller & Spielhagen, 1990). The Basilika formation is thought to have been deposited in a periodically anoxic (Müller & Spielhagen, 1990) pro-delta shelf setting, more distal than their underlying sediments (Steel et al., 1981; Nagy et al., 2000), during a time of methane seepage (Hryniewicz et al., 2016). The Grumantbyen formation shows a change from the transgressive trend in the previous two formations to a regressive trend, with sediments transitioning from marine shales into marine glauconite sandstones that are heavily bioturbated (Steel et al., 1981). Both the Firkanten and the Basilika formation contain bentonite layers in their strata (Dypvik & Nagy, 1978). They described the bentonite layers as very fine grained, poorly sorted deposits, consisting about 80% of clay minerals related to altered, wind-transported volcanic material. Coal seams have been found by Major & Nagy (1972) both above and under the Basilika formation in the

Eocene Aspelintoppen Fm, the Paleocene Firkanten Fm, and the Lower Cretaceous Helvetiajellet Fm. Potential source rocks for petroleum are situated in Paleozoic and Mesozoic sequences, in (dark) shales, siltstones, and micritic carbonaceous beds (Major & Nagy, 1972). Potential cap rocks for the petroleum are found in the Triassic, Jurassic, and Cretaceous as shales, but also in the Tertiary as plastic clay beds (Major & Nagy, 1972).

During the Early Cretaceous Spitsbergen experienced intrusive and extrusive magmatism contemporaneously with widespread volcanism throughout a large part of the Arctic related to the formation of the High Arctic Large Igneous Province (HALIP), which persisted from the Cretaceous to the Paleocene (Maher, 2001; Tegner et al., 2011). In the Late-Cretaceous and Paleocene the HALIP extruded an alkaline suite through continental rifting (Tegner et al., 2011). Volcanism ceased in the Paleocene when rifting was replaced by compression (Tegner et al., 2011). Elling et al. (2016) found that the bentonites in the Firkanten and Basilika formations originate from alkaline continental-rift magmatism and were deposited with a dominant sediment supply from the east. From radiometric ages, biostratigraphy, and lithostratigraphic correlations of, and around, the Basilika formation, Elling et al. (2016) estimated an age between 62-58 Ma for the deposition of this formation, placing it between the Late Danian and Early Thanetian.



Figure 2. Shapes of a few glendonite samples and type of surrounding sediment. Glendonite found nearby a bentonite layer (A), 2 to about 8 cm glendonite samples with rosette shape (A-E). Shell fragment nearby glendonite (C).

Methods

Thin section analysis

A drilling core (BH1-2004, Fig. 2) was taken across the whole Basilika formation nearby Sveagruba on Spitsbergen (Fig. 3). This formation spanned 133 m in core length and contained glendonites. Sampling of this core was done from old to young, i.e. sample BH2 is located near the Firkanten-Basilika transition and BH40 is located near the Basilika-Grumantbyen transition. Thin-sections were made from 16 glendonite samples throughout this core and subsequently analysed for their petrography using a Leica DM 2500 LED microscope with plane-polarized light at 200x magnification and 1000x magnification. For the 1000x magnification immersion oil was used to obtain a sharper image of the thin section. Macrostructures have been largely ignored, as the samples show little of those, instead the focus was on the microstructures. Previous studies have described the petrography of glendonites and found multiple types of carbonates reflecting different generations of their formation (e.g. Larsen, 1994; Greinert & Derkachev, 2004; Huggett et al., 2005; Teichert & Luppold, 2013; Morales et al., 2017; Qu et al., 2017; Vickers et al., 2018; Bloem, 2019; Vickers et al., 2020). Most of these authors distinguished three carbonate generations and dubbed these as type 1, type 2, and type 3.

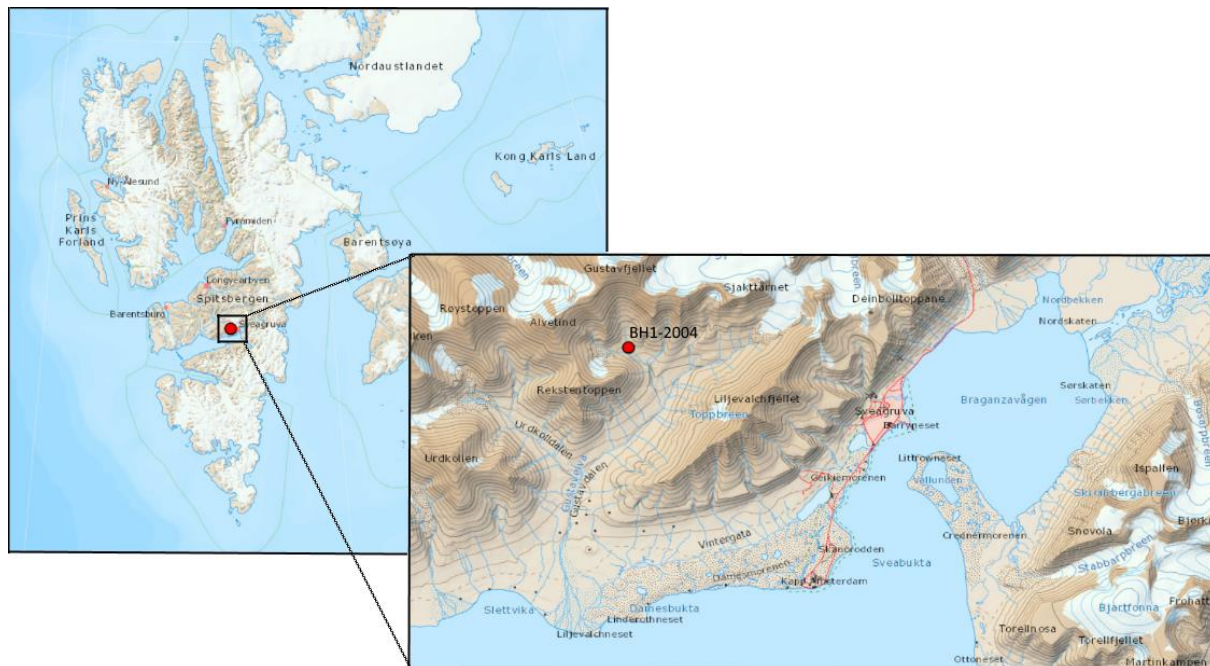


Figure 3. Map of Svalbard showing the location of the drilling core BH1-2004 (Modified from the Norwegian Polar Institute, 2022).

Type 1 has been found in all of the previously mentioned petrographic studies and often consists of white or transparent calcite crystals, oval or irregular in shape. This generation typically shows little twinning, and is often inclusion-rich. Other names given to this generation are primary calcite (Greinert & Derkachev, 2004), rosettes (Morales et al., 2017; Bloem, 2019), and replacive calcite (Teichert & Luppold, 2013; Qu et al., 2017). Bloem, 2019 has also identified a type 1b, which he dubbed the Rov phase. He describes this generation as fibrous calcite overgrowing the type 1 generation.

Type 2 calcite is also occurring in all glendonites from previous mentioned petrographic studies. This generation is described as fibrous and spherulitic (Huggett et al., 2005), isopachous (Teichert & Luppold, 2013), botryoidal (Vickers et al., 2018), or fibrous to botryoidal (Morales et al.,

2017) calcite rim cement, in some studies yellow to brown-coloured (e.g. Huggett et al., 2005; Morales et al., 2017; Vickers et al., 2018). In Bloem (2019) this generation is named the Bot phase.

Type 3 is identified as a sparry calcite (Larsen, 1994; Huggett et al., 2005; Vickers et al., 2018), yellow to brown or transparent (Morales et al. 2017; Vickers et al., 2018), which acts as a cement to fill in pore spaces (Huggett et al., 2005; Teichert & Luppold, 2013). This generation is found to be a clear (Huggett et al., 2005) or anhedral (Morales et al., 2017) spar. Bloem (2019) found white coloured calcite for this generation and dubbed this calcite cement. Bloem (2019) also identified a yellow calcite generation similar to the type 3 of Morales et al. (2017).

In this study the classifications for glendonite generations will be evaluated for the glendonite thin sections from the Paleocene of Spitsbergen and a classification that best fits the results of this study will be chosen or made.

High-resolution composition analysis

Two thin sections were analysed using Raman spectroscopy to determine the phases and potential composition of the inclusions within the glendonites. This technique uses the inelastic scattering of photons, caused by the interaction with atoms of a material (Wolverson, 2008). Some of these inelastically scattered photons promote or suppress vibrations of the atoms, where the resulting energy of the photon is directly related to the energy required for the vibration transition (Wolverson, 2008). The range of vibrational modes is unique for different materials and the energy of these modes reflects the material's chemistry. Therefore, the Raman shift of the scattered photons can be related to the chemical structure of the analysed material. The laser emitting the photons used in this study was a He-Ne laser with a wavelength of 785 nm. To correct for the spectral drift in the machine a silicon standard was used. The Raman spectrometer was connected to a Raman microscope and the charge coupled device camera used to capture the photons was cooled to -60°C. This study focused on investigating the inclusion content and the calcium carbonate phase of the type 1 generation of the glendonite. For this purpose a 100x objective on the microscope was used to select a line across inclusions and the type 1 generation to analyse with the Raman technique. To find inclusions a 3D view was obtained by scanning multiple lines over a depth transect of 10 µm. An overview image of the studied section was obtained by using transmitted plane-polarized light in the microscope.

Biomarker analysis

To find further clues about ikaite formation and its transformation to glendonite, the organic molecular composition of both the glendonites as well as the sediments around them were analysed. Core samples of glendonites with sediment were crushed and separated in two steps. In the first step the core sample was crushed into pieces of cm-scale and subsequently picked by hand to separate the glendonite from the sediment. The smaller pieces were checked with the assistance of a stereomicroscope to see if errors were made in separating. The pieces that were not separated correctly were split again by crushing and separated by hand in the second step. Both sediment and glendonite samples were ground as fine as possible with an agate pestle and mortar. The weights were aimed to be in between 20 to 35 g for both sediment and glendonite samples, but for some samples this could not be reached. For two glendonite samples (sample codes BH15Cg and BH18Cg) the amounts were below 10 grams, so these were combined together for biomarker analysis. The glendonites used for biomarkers spanned 13 meters of core depth in between 39 and 52 m from the bottom of the Basilika formation, while the sediment samples came from throughout the core. Once the sediment was ground, the biomarkers were extracted from the grains through Soxhlet extraction, using DCM:MeOH (dichloromethane:methanol) 7.5:1 as solvent for 24 hours. Boiling stones were used to speed up the process. The solvent was then evaporated through a BUCHI Rotavapor R-114 in

water of around 40°C leaving the biomarkers behind in the flask. A new solvent DCM:MeOH 9:1 was

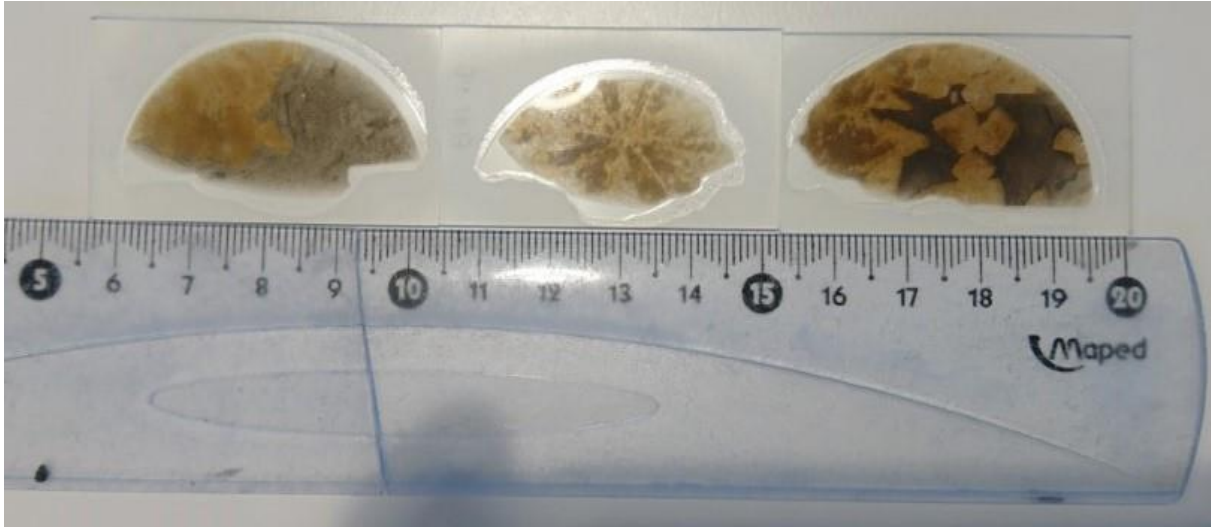


Figure 4. Macrostructure of glendonites. These samples are amongst the ones used for biomarker analysis. From left to right: BH19B; BH16B; BH14B.

used in small amounts to dissolve the biomarkers. The samples had their remaining water removed by pipetting the dissolved biomarkers through a Na_2SO_4 column into 4 mL vials. The solvent was subsequently evaporated using a nitrogen blaster at about 30°C heating leaving only the total lipid extract (TLE) behind in the vials. For successful splitting of the polar and apolar fractions, a 4 cm aluminium oxide column with a maximum of 5 mg TLE had to be used. In the cases where the total lipid extract was greater than 5 mg it was split using a known amount of DCM:MeOH 9:1 to dissolve the TLE and then pipetting an amount which would have less than 5 mg of TLE in it. This was then dried again by the nitrogen blaster before further extraction. The dry TLE was then split into the polar and apolar fractions, with the apolar fraction being the first to be extracted through the aluminium oxide column into 4 mL vials. A Hexane:DCM 9:1 solvent was used to dissolve the apolar fraction. After the apolar fraction was extracted, a DCM:MeOH 1:1 solvent was used to extract the polar fraction. Both fractions were then dried again using the nitrogen blaster. The apolar fraction was then dissolved in a known amount of hexane and measured in a gas chromatograph. The polar fraction was treated for liquid chromatography to see if there are any GDGTs inside. This was done by dissolving it in a known amount of Hexane:Isopropanol 99:1 solvent and adding a GDGT standard to the sample. The GDGT standard is necessary to be able to quantify the GDGTs if there are any present. As the liquid chromatograph used in this study is tuned for GDGT analysis, the non-GDGT fraction cannot be determined. Therefore, a focus is laid on the apolar fraction in this study. Next to the core samples in this study, a sample (SVEA-1) sampled in a previous study by den Boer, 2019 was also analysed for biomarker content. This sample comes from a mud volcano on Spitsbergen of Paleocene age, also from the Basilika formation.

Results

Structure

The glendonites present in the drill core were about 2 to 8 cm in diameter, usually with a rosette shape (Fig. 2). The glendonites were found to be surrounded by clay-rich sediment and sometimes in the presence of a nearby bentonite (Fig. 2A) or fossil (Fig. 2C). The thin sections show little mentionable in the macrostructure of glendonites (Fig 4). The glendonites are usually orange-yellow to white coloured, while the sediment is black to gray in colour.

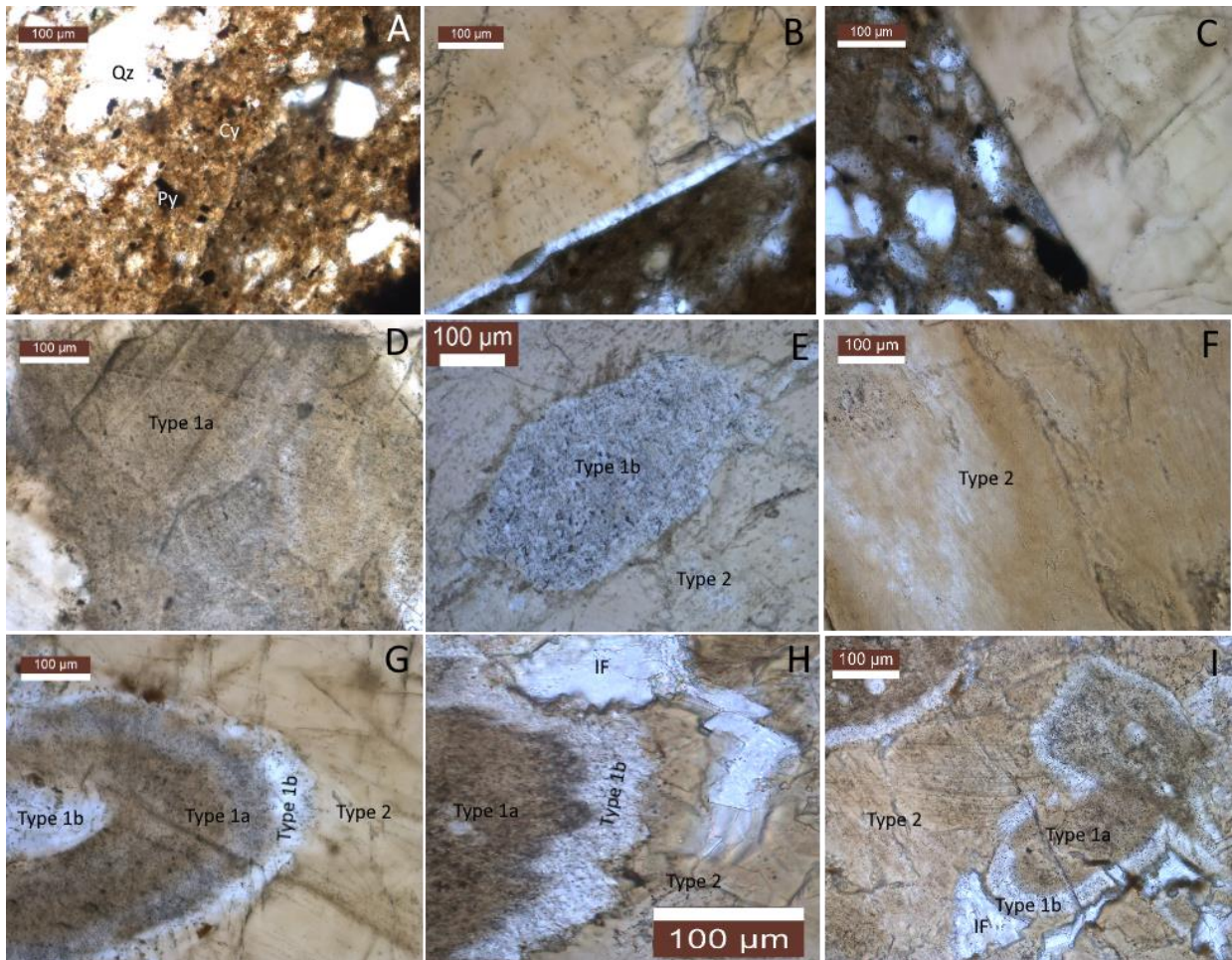


Figure 5. Microstructures of glendonites at 200x magnification. Sediment around glendonite containing pyrite (Py), quartz (Qz), and orange to gray clay (Cy) (A); Boundary between glendonite and sediment (B-C); Yellow and white glendonite with a high amount of inclusions (Type 1a, (D)); White glendonite crystal with a moderate amount of inclusions (Type 1b) surrounded by a sparry yellow glendonite crystal with few inclusions (Type 2, (E)); Yellow to white glendonite crystals with fibrous texture (Type 2, (F)); Type 1b with botryoidal or spherulitic shape rimming a yellow or white/gray type 1a (G-I); White euhedral to anhedral calcite infilling (IF, H-I).

Microscopic observations confirm that the sediment consists mainly of quartz crystals, blocky pyrite crystals, and a gray and yellow to orange mass of clay crystals (Fig. 5A). The boundary between the glendonite and sediment is sometimes made up of a fibrous white rim around part of the border of the glendonite (Fig. 5B), but usually lacks the rim and instead the border of the glendonite with the sediment often consists of a yellow-coloured sparry calcite (Fig. 5C). There are also cases where this border consists of a white calcite containing inclusions, or a gray calcite full of inclusions, albeit these appearances are less ubiquitous. In general, three main types or generations of glendonite crystals can be identified (Fig. 5D-F). The first type is a yellow or gray to white glendonite crystal very rich in inclusions and without a clear crystal texture (Fig. 5D). This type is referred to as type 1a in this study. The second type, called type 1b in this study, is a glendonite crystal with a moderate to low amount of inclusions which shows more of the glendonite crystal than type 1a (Fig. 5E). This generation usually has white glendonite crystals (Fig. 5E), but sometimes also occurs as yellow crystals (Fig. 6B). The crystals of this type are found as solitary pieces (Fig. 5E) or as rims around type 1a (Fig. 5G-I, 6A). When this generation occurs as rims it often has a spherulitic (Fig. 5G, 5I) or botryoidal shape (Fig. 5H). In Fig. 6A-D the inclusions in the type 1b generation appear to have an orientation in the same direction as the crystal orientation, in a fibrous manner. The crystal of type 1b itself sometimes has a clear fibrous texture with little to no inclusions (Fig. 6A). The third glendonite generation, named

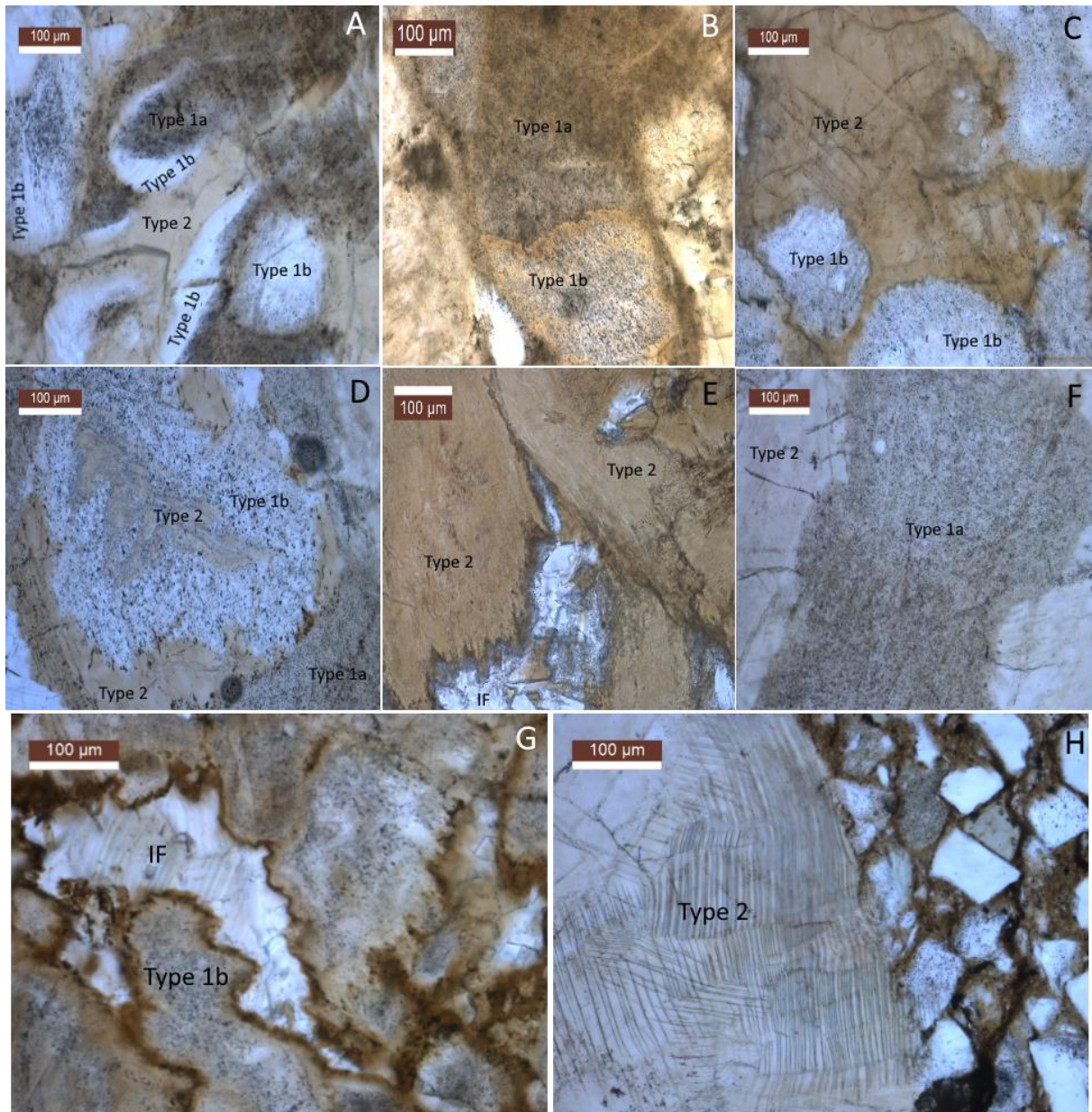


Figure 6. Microstructures of glendonites at 200x magnification. Fibrous type 1b with little to no inclusions and type 1b with a moderate amount of inclusions (A); Yellow and white type 1b with an orientation of the inclusions in a fibrous manner (B); Type 1b with little inclusions together with type 1b with a moderate amount of inclusions (C); Type 1b crystal with type 2 inside and outside (D); Fibrous yellow type 2 and white infilling (E); White type 1a and type 2 (F); Orange sediment in cracks between crystals (G); Diagenetically altered type 2 with clear fibrous twinning (H).

type 2 in this study, is made up of a sparry carbonate with little to no inclusions, often yellow of colour (Fig. 5F), but also occurring with a whiter colour (Fig. 6F, 6H). This generation often shows a fibrous texture (Fig. 6E, 6H), but this is not always recognizable. This generation is usually the most abundant one in the glendonite samples. In Fig. 6D a type 2 generation is seen within and outside of a type 1b generation where the type 1b seems to gradually decrease in inclusions and white colour towards the type 2 within. In some glendonites there is another carbonate type present appearing as euhedral or anhedral angular white crystals without the fibrous texture and inclusions, referred to as carbonate infilling or IF (Fig. 5H, 6E, 6G). The glendonite samples in this study are sometimes fractured or cracked. These openings are often filled with sediment, at times orange of colour (Fig. 6G) similar to the orange clay. Diagenetic twinning happens in the shape of the fibrous texture (Fig. 6H). The 1000x magnification on the three growth generations show changes in the inclusions

depending on the focus and zoom of the microscope (Fig. 7). The blue hue is probably due to the oil used on the thin-sections. From an out-of-focus zoomed-out position the inclusions are brown-coloured and round (Fig. 7A). This roundness is related to the low focus. In a high focus and greater zoom the inclusions are black of colour and less rounded (Fig. 7B). When zoomed in further the inside of inclusions is shown to be transparent, with a black outer edge (Fig. 7C). There is a small white rim around the inclusions.

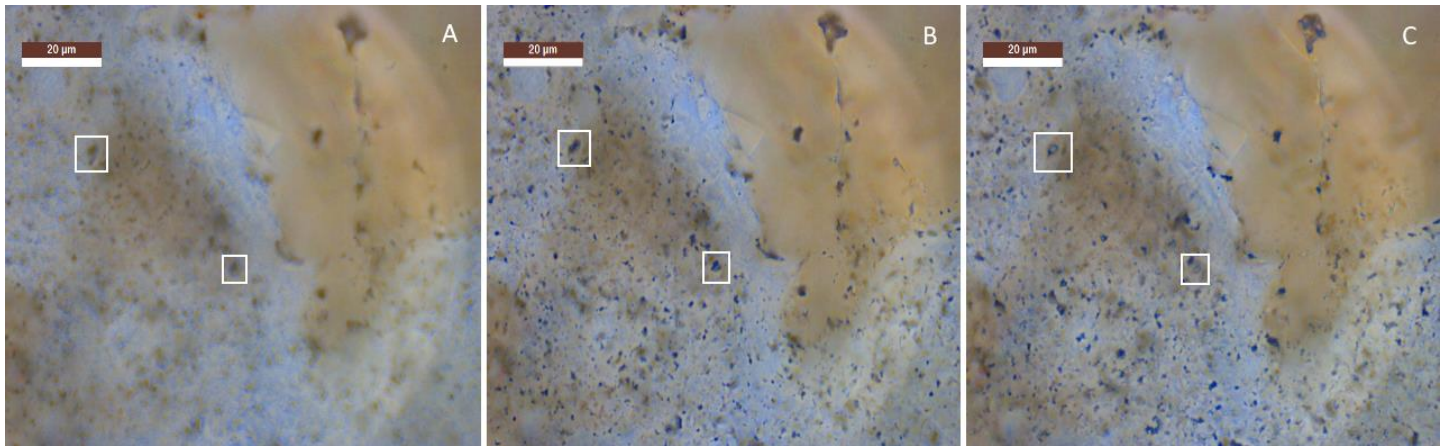


Figure 7. 1000x magnification of type 1a, type 1b, and type 2 generations at various zoom and focus levels. White squares highlight specific inclusions, changing in appearance through the different zoom and focus levels. In (A) the inclusions are brown-coloured, in (B) they are black coloured, and in (C), when zoomed in further, they are transparent with a black outline.

Chemical composition

The overview images of the glendonite (Fig. 8A) show that the line analysed with Raman spectroscopy for chemical composition was drawn over the type 1a generation with at places more calcium carbonate visible, identified by the white colour, and at other places less, represented by the darker colour (Fig. 8A). This image only shows the glendonite at the surface, so underneath the composition could be different and inclusions can be found (Fig. 8B). In all intensity maps on the line there is a peak at around Raman shift 1086 cm^{-1} (e.g. Fig. 8C-E), consistent with the symmetrical stretching found within calcite (DeCarlo, 2018, Fig. 9). It is expected that the white calcium carbonate in type 1a contains calcite while the inclusions are expected to lack calcite. Therefore, the Raman spectra have been filtered on the calcite band to produce an intensity map where the lighter colours indicate the presence of calcite and the darker colours the absence of calcite, which can be used to identify the inclusions (Fig. 8B). Two locations have been selected in the glendonite, one at the surface in the white calcium carbonate (Fig. 8B1), the other at an inclusion deeper into the glendonite (Fig. 8B2). From the Raman spectra of both these locations a huge background signal is found to overprint most of the vibrational modes (Fig. 8C). Removing the background showed that there is a clear peak at around Raman shift 1086 cm^{-1} and a very broad envelope containing multiple bands in between Raman shifts 1200 and 1500 cm^{-1} (Fig. 8D). The peak at 1086 cm^{-1} is clearly seen in the zoomed-in raw Raman spectrum (Fig. 8E). In the Raman spectrum of the white carbonate there is also a peak identifiable at around a Raman shift of 282 cm^{-1} (Fig. 8D1), also related to calcite (DeCarlo, 2018). Vaterite has a doublet at 1080 and 1090 cm^{-1} , rather than a singlet at 1086 cm^{-1} (Wehrmeister et al., 2009, Fig. 9). As all the spectra showed a single band at 1086 cm^{-1} , no vaterite was detected in these samples. Type 2 and type 1b generations were also analysed and similar peaks with high background were found (Appendix A1-2 respectively). Due to the high background these spectra show very little information on the presence of other compounds. As there was a high background, only two glendonite samples were analysed.

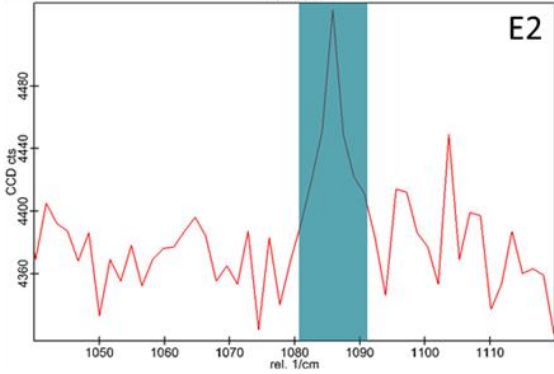
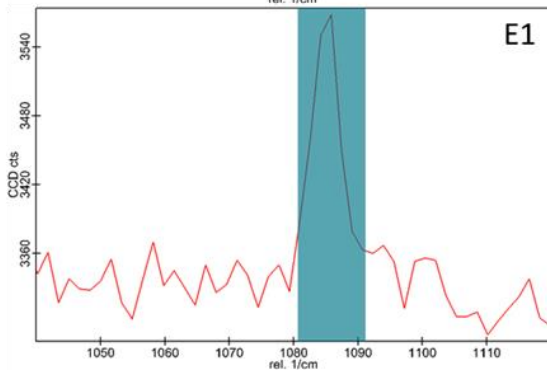
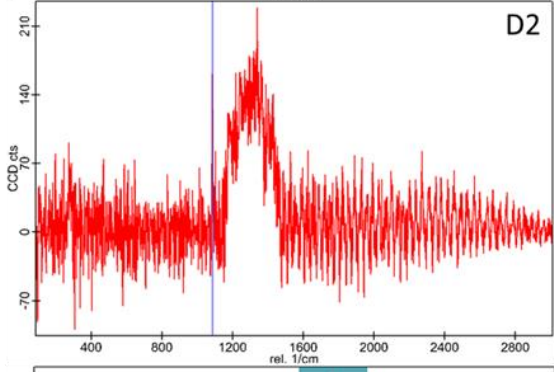
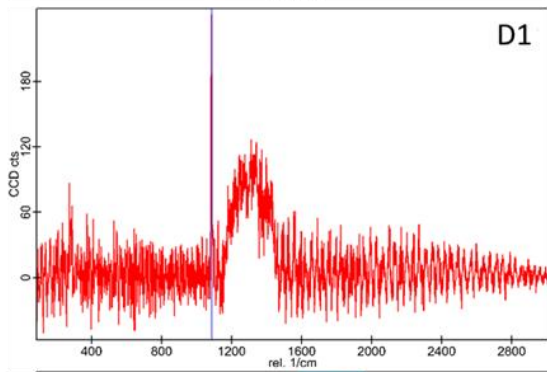
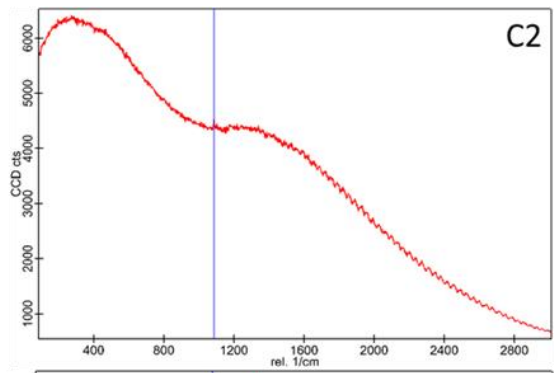
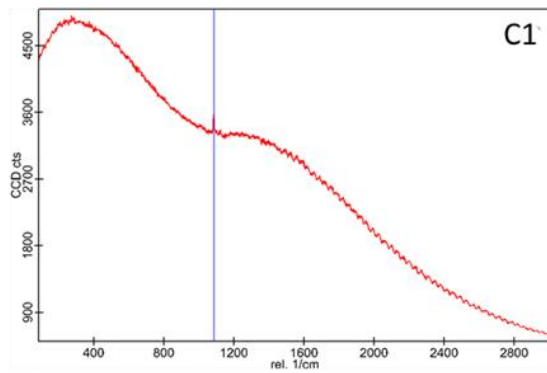
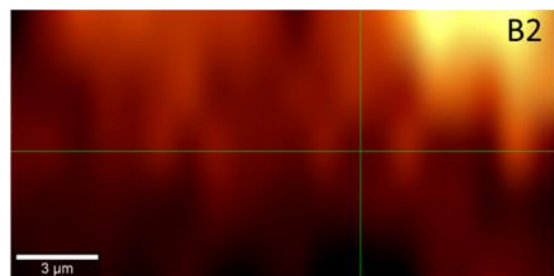
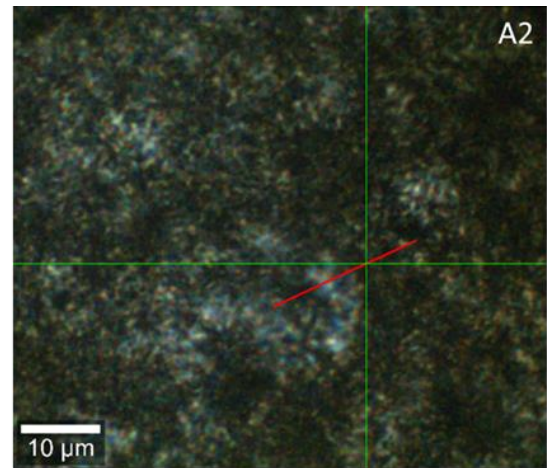
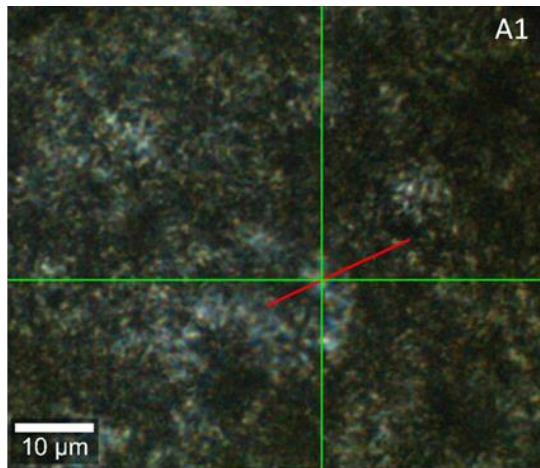
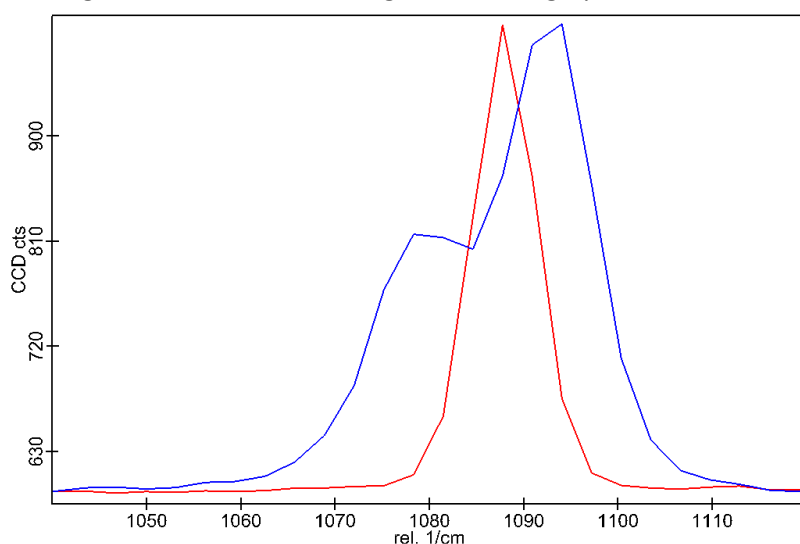


Figure 8. Raman spectrum of the white calcium carbonate of the type 1a generation (1) and of a suspected inclusion (2). Type 1a as viewed under the microscope with transmitted plane-polarized light (A). The red line is the transect over which Raman spectra have been made, the green crosshair shows the position on the line at which the analysed white calcium carbonate is found. Intensity map of the materials highlighted by the blue area over the transect of the red line (B). High amount of counts of this material are shown by a lighter colour, low amount of counts of this material are shown by a darker colour. Complete Raman spectrum at the position of the green crosshair (C). Raman spectrum with subtracted background (D). Peak in the raw Raman spectrum at the highlighted blue area (E). The black line is there to clearly separate the two Raman spectra

Organic Geochemistry

The apolar fractions of the glendonites and sediments look very similar with the most important peaks being present in both types of sample from the Paleocene drilling core (Fig. 10-11). These chromatograms show a clear n-alkane distribution with unsaturated hydrocarbons present in lower amounts. The spectrum of mass 183 is shown in the subplot of Fig. 10A and corresponds to pristane, which is found in all glendonite and sediment samples. Phytane is also found in all glendonite and sediment samples but in lesser amounts than pristane. In the subplot of m/z 192 it is seen that the second peak in the mass spectrogram corresponds to the red peak in the chromatograms of the samples. This peak represents methylphenanthrene (Huang et al., 2016). The peak of methylphenanthrene is missing in the glendonite sample from the mudvolcano (Fig. 12). Squalene is found in most samples, both sediment and glendonite, from the drilling core as well as from the mud volcano, in abundances ranging from very high (Fig. 10), to low (Fig 12), to absent (Fig 11). Squalene is produced by plants and animals as precursor for sterols (Micera et al., 2020). This peak in squalene could be explained by squalene derived from human skin (Micera et al., 2020) contaminating the samples, probably during the separation of the sediments from the glendonites. No other significant contaminants have been found in the chromatographs. There is no clear difference in biomarkers between glendonites and their surrounding sediment (Fig. 10B-C) or between sediments from the glendonite horizon and sediments below or above this horizon (Fig. 10-11). The molecular composition of the bentonite is unlike that of the glendonites or sediments from the same core (Fig. 13). The distribution of saturated hydrocarbons in the bentonite is very different compared to the sediment or glendonite distribution, and some expected hydrocarbons are even missing. From the bentonite biomarkers a large peak representing methylphenanthrene is seen. Furthermore, there is a huge unresolved complex mixture (UCM) present in this sample which makes determining the molecular content of this sample difficult. The retention times of specific molecules in the chromatograms of Fig. 10 and Fig. 12 are different compared to the chromatograms in Fig. 11 and Fig. 13 because a different gas chromatograph was used to measure the samples from Fig. 11



and Fig. 13 than the samples in Fig. 10 and Fig. 12. Other glendonite and sediment chromatograms from this study are found in Appendix B. The polar fraction of the glendonites and sediments showed no GDGTs and in some cases a

Figure 9. Synthesized Calcite (red) and synthesized vaterite (blue) Raman spectra. The calcite peak is at Raman shift 1087 cm^{-1} , the two vaterite peaks are at around Raman shifts 1080 cm^{-1} and 1090 cm^{-1} .

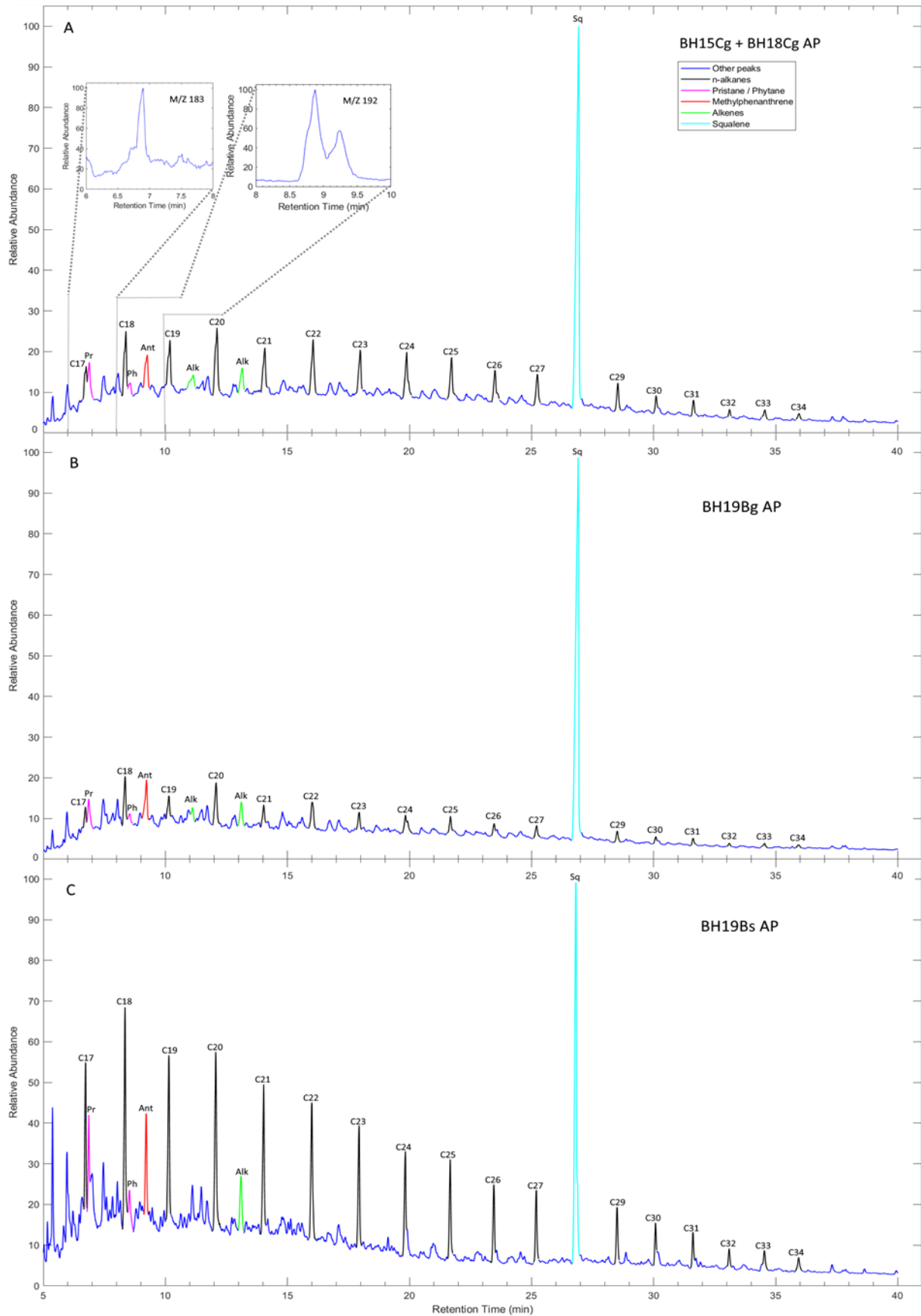


Figure 10. Gas chromatograms for two glendonite samples (A-B) and one sediment sample cut out from around the glendonite BH19Bg (C) from the Paleocene drilling core. The apolar fraction was analyzed for all these samples. Pr = pristane, Ph = phytane, Ant = methylphenanthrene, Alk = alkenes, Sq = squalene, and C17-C34 correspond to n-alkanes with their respective carbon atom number.

small peak in crenarchaeol (results not shown).

The abundance of pristane and phytane from the same samples can be used to calculate the pristane to phytane ratio (Table 1). This ratio can be used to reconstruct paleoenvironmental conditions (Peters et al., 2004). The average Pr/Ph ratio for the sediment and glendonite samples of the drill core are 3.62 and 3.23 respectively. The value for the SVEA-1 sample is 1.82, which is much lower than any of the samples from the drilling core. From the n-alkane distribution the carbon preference index (CPI) can be calculated. This index is used to find the biological origin of the n-alkanes, the maturity of oils or source rock extracts, and/or to reconstruct paleoenvironmental conditions (Herrera-Herrera et al., 2020). The CPI was first introduced by Bray and Evans (1961) but was revised by various authors such as Marzi et al. (1993) to give better results. In this study I use the generalized formula of the CPI by Marzi et al. (1993):

$$CPI = \frac{(\sum_{i=n}^m C_{2i+1}) + (\sum_{i=n+1}^{m+1} C_{2i+1})}{2 \cdot (\sum_{i=n+1}^{m+1} C_{2i})} \quad (1)$$

Where n = starting n-alkane divided by 2, m = ending alkane divided by 2, and i = index. The n-alkanes between carbon number 17 and 34 are present in all glendonite and sediment samples (e.g. Fig. 10-12), with the exception of the 28-alkane which is masked by the squalene peak in some samples (Fig. 10-12). For the samples with a masked 28-alkane a value will be given in the middle between the value of the 27-alkane and 29-alkane as this estimation would follow the general trend of the n-alkane distribution this way (Fig. 10-12). The CPI in this study will use n = 8 and m = 15 to span the range of C17 to C33 and the following equation will then be obtained:

$$CPI = \frac{(C17 + C19 + C21 + C23 + C25 + C27 + C29 + C31) + (C19 + C21 + C23 + C25 + C27 + C29 + C31 + C33)}{2 \cdot (C18 + C20 + C22 + C24 + C26 + C28 + C30 + C32)} \quad (2)$$

Table 1. CPI and Pr/Ph ratios.

Sample code	Material	Pr/Ph ratio	CPI	Estimated 28-alkane*
BH2-2 AP	Sediment	2.59	0.98	no
BH11 AP	Sediment	3.62	0.98	no
BH14 AP	Sediment	5.08	0.97	no
BH14Bg AP	Glendonite	3.05	0.88	yes
BH15Cs-2 AP	Sediment	2.88	1.05	no
BH16Bs-2 AP	Sediment	3.45	1.06	no
BH16Bg AP	Glendonite	2.91	0.85	yes
BH18Cs-2 AP	Sediment	3.27	1.07	no
BH15Cg + BH18Cg AP*	Glendonite	3.61	0.85	yes
BH19Bs AP	Sediment	2.59	0.91	yes
BH19Bg AP	Glendonite	3.37	0.81	yes
BH28-2 AP	Sediment	3.26	1.01	no
BH40 AP	Sediment	5.82	0.97	no
SVEA-1 AP	Glendonite	1.82	1.06	no
Average BH sediment	Sediment	3.62	1.00	x
Average BH glendonite	Glendonite	3.23	0.85	yes

*This column is to indicate if the 28-alkane was estimated for calculation of the CPI

*This is a mixed sample containing glendonite material from sample BH15Cg and sample BH18Cg

The average CPI values for the sediment and glendonite samples from the drilling core are 1.00 and 0.85 respectively (Table 1). Since the area of the 28-alkane had to be estimated for one sediment sample and all glendonite samples, the CPI calculated is an approximation of its true value. Nevertheless, the error on the CPI due to estimation of the 28-alkane is not expected to be great. The SVEA-1 sample has a CPI of 1.06, similar to that of the drilling core samples (Table 1).

Discussion

Oil migration in the Basilika Formation

The CPI for the sediment and glendonite samples are around the 1 or even slightly below, indicative

of crude oil (Bray & Evans, 1961). This relation with oil is strengthened by the presence of both pristane and phytane, which are generally linked to oil, coal, and sediments that can act as a source rock for petroleum (e.g. Johns et al., 1966; Brooks et al, 1969; Powell & McKirdy, 1973). Pristane and phytane are isoprenoid hydrocarbons which are mainly formed from the phytol side chain of chlorophyll (Brooks et al., 1969), but other sources are also possible (e.g. Blumer et al., 1963; Nissenbaum et al., 1972). During diagenesis, the phytol side chain is cleaved to form phytol (Brooks et al., 1969). When this happens during anoxic or reducing conditions the phytol is reduced to dihydrophytol which is then reduced to phytane (Peters et al., 2004). During oxic conditions the phytol is oxidized to phytanic acid which subsequently undergoes decarboxylation to form pristane (Peters et al., 2004). Brooks et al. (1969), therefore, suggested that the ratio of pristane over phytane can be used as proxy for oxygen content of the sediment environment during diagenesis. However,

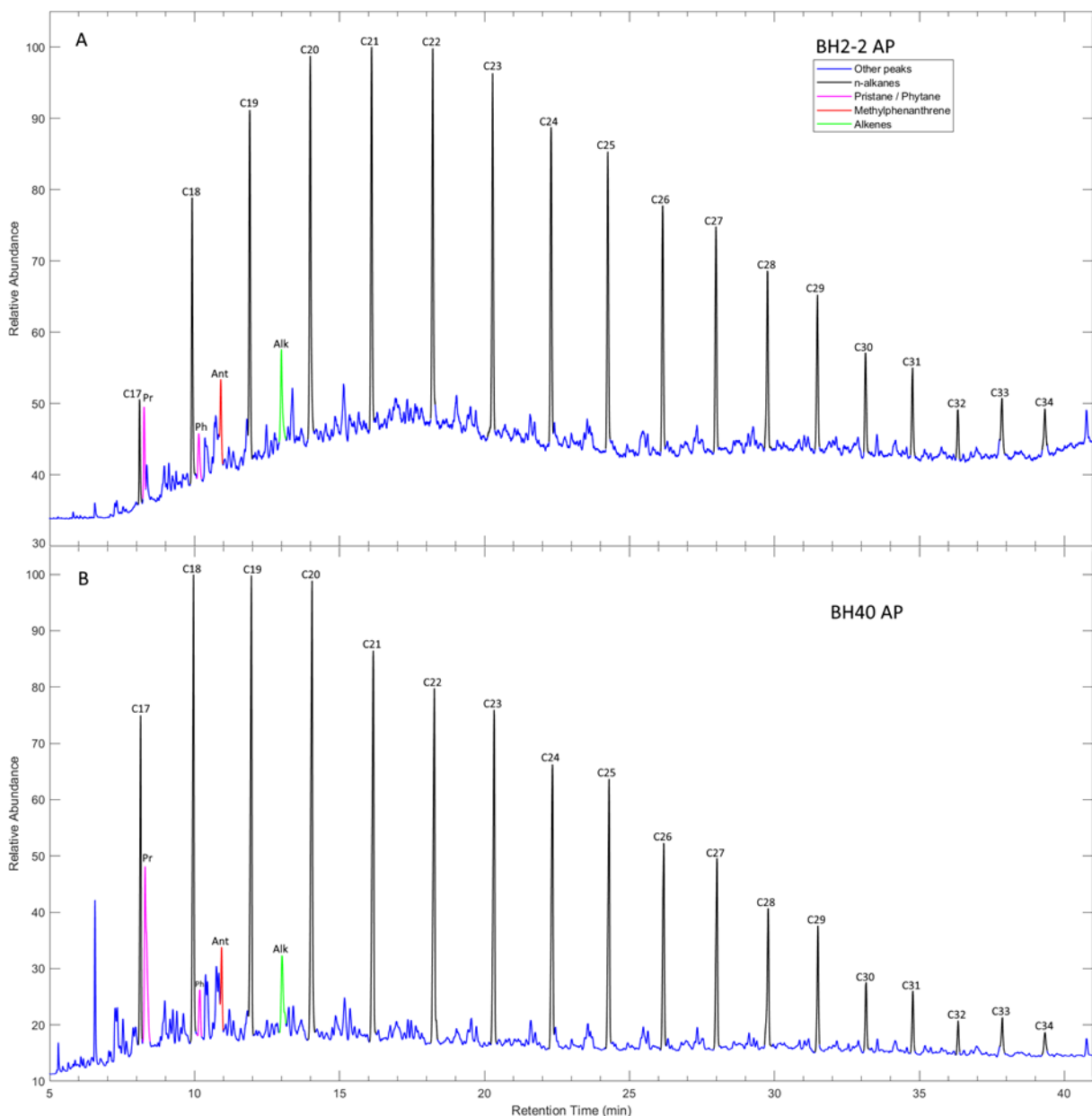


Figure 11. Gas chromatograms of sediment samples below (A) and above (B) the glendonite horizon of the Paleocene drilling core. The apolar fraction is shown. Pr = pristane, Ph = phytane, Ant = methylphenanthrene, Alk = alkenes, and C17-C34 correspond to n-alkanes with their respective carbon atom number.

the direct use of this ratio to reconstruct paleoenvironmental conditions is limited by several factors as described by Peters et al. (2004). This includes a variable source input, analytical uncertainties, and different rates of formation of phytane and pristane in low maturity as opposed to high maturity oils, as well as in extracts from source-rocks. Thus, the pristane/phytane ratio is not only affected by oxygen conditions. Peters et al. (2004) recommends the use of the pristane/phytane ratio for paleoenvironmental reconstruction only for values <0.8 to indicate saline to hypersaline conditions related to carbonates and evaporites, and values >3.0 to indicate oxic to suboxic conditions and terrigenous plant input. The drilling core sediment and glendonite samples have Pr/Ph ratios mostly between 2.5 and 3.5, with few samples having significant higher Pr/Ph ratios. The average Pr/Ph ratio for all the sediment and glendonite samples of the drilling core is greater than 3.0, making the use of this ratio for paleoenvironmental reconstruction more robust. This ratio suggests that the samples from the drilling core were deposited during oxic to suboxic conditions with terrigenous plant input. This is nonconform to the idea of a periodically anoxic environment from Müller & Spielhagen (1990). An oxic depositional environment also contradicts the hypothesis that ikaite is mainly driven by anaerobic oxidation of carbon species (e.g. Teichert & Luppold, 2013; Morales et al., 2017; Qu et al., 2017; Vickers et al., 2018; Bloem, 2019). The presence of black shales and high abundances of pyrite in the sediment also point toward anoxic conditions (Steel et al., 1981; Müller & Spielhagen, 1990). With this in mind and also the fact that the average Pr/Ph ratio is close to 3 and thus potentially unreliable (Peters et al., 2004), the conditions for formation were likely not oxic but rather suboxic to anoxic.

Most remarkable from the biomarker data is the presence of the polycyclic aromatic hydrocarbon (PAH) methylphenanthrene found in all the drilling core samples (Fig. 10-11, 13). PAHs are produced through four generalized pathways: diagenetic alteration of organic matter, formation of petroleum and coal, pyrolysis of biomass, and biosynthesis by plants and animals (Boehm, 2005). PAHs, when formed as a diagenetic product of microorganisms or when biosynthesized by plants or animals, have a simple composition (i.e. low amount of variation in aromatic rings in the structure) with only few PAH species (Boehm, 2005). PAHs originating from the formation of petroleum and coal are called petrogenic PAHs and form at moderate temperatures (100-300°C) and elevated

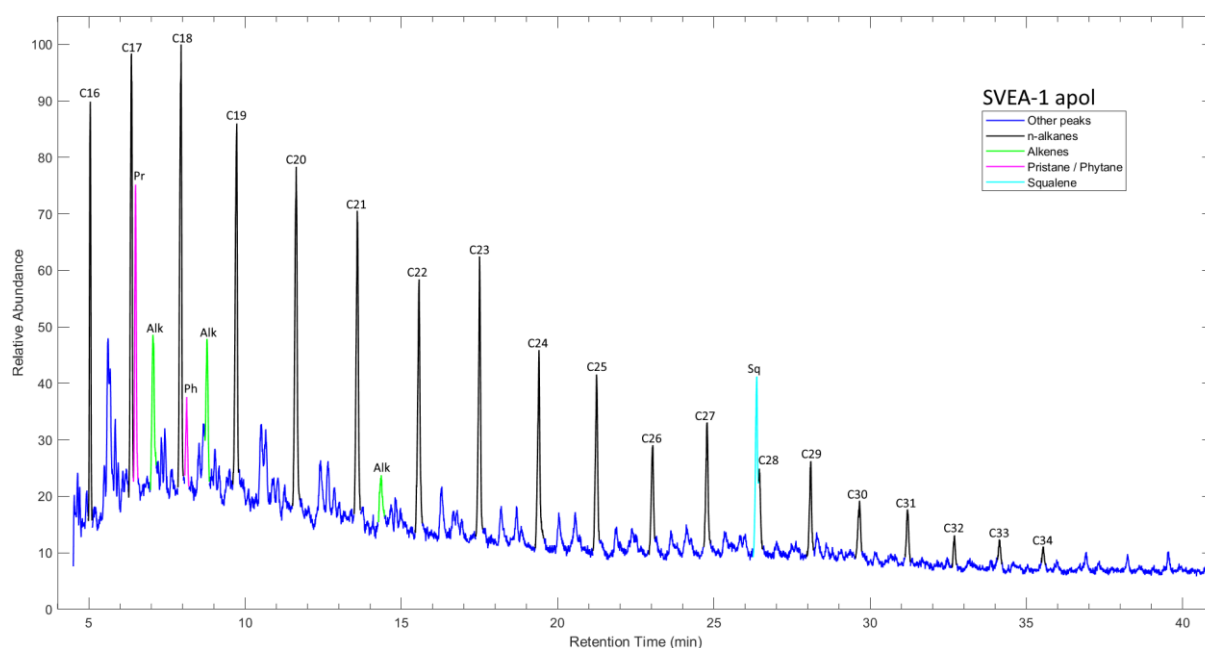


Figure 12. Gas chromatogram of a glendonite sample from the mud volcano of Paleocene age. Pr = pristane, Ph = phytane, Alk = alkenes, Sq = squalene, and C16-C34 correspond to n-alkanes with their respective carbon atom number. Data from den Boer (2019).

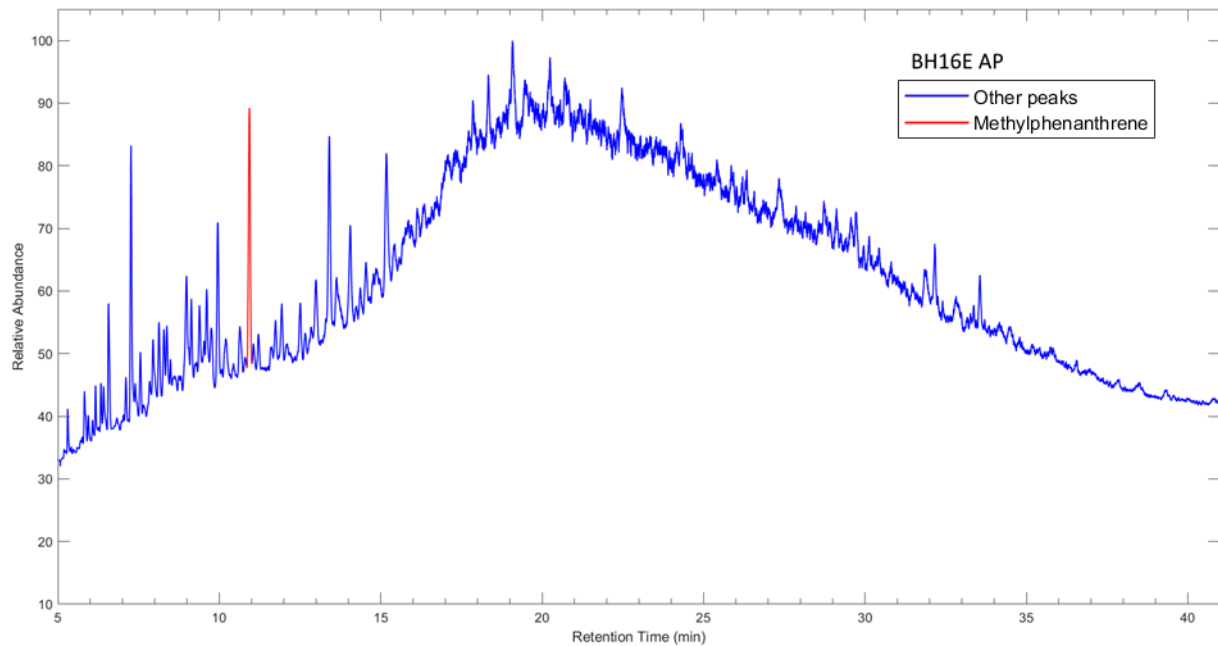


Figure 13. Gas chromatogram of a bentonite sample from the Paleocene drilling core.

pressure (Boehm, 2005). Petrogenic or pyrogenic PAHs contain an assemblage of multiple complex (i.e. high amount of variation in aromatic rings in the structure) PAH species (Boehm, 2005). Crude oils and coals have a similar composition of PAHs but differ from each other in the amount of PAHs: PAHs only make up a small fraction (0.2-7%) of a typical crude oil, while in typical coals this is some fractions smaller (<0.02%, Boehm, 2005). Petrogenic PAHs have a higher relative abundance of alkylated PAHs compared to parent PAHs, as opposed to pyrogenic PAHs, which have a higher abundance of parent PAHs relative to alkylated PAHs (Boehm, 2005). Methylphenanthrene is an alkylated PAH and is more abundant than the lacking parent molecule, phenanthrene, suggesting a petrogenic source. However, methylphenanthrene can come from both the diagenetic pathway as well as the petrogenic pathway (Boehm, 2005). Methylphenanthrene produced through the diagenetic pathway is only formed in trace amounts (Boehm, 2005), making the petrogenic pathway the most plausible source for this compound in this study.

The most likely origin of methylphenanthrene in this study is the coal deposit in the Firkanten formation or the source rock in the Cretaceous, which can contain crude oil (Major & Nagy, 1972). The cap rock in the Cretaceous (Major & Nagy, 1972) would prevent oil from reaching higher sediment layers, thus making it unlikely for the oil in the Basilika formation to be sourced from sediments below the cap rock. Coals have the potential to generate both oil and low molecular weight volatile hydrocarbons, but will yield more hydrocarbons than oil (Tissot & Welte, 1978). Nevertheless, oil produced from coal has the potential to migrate through sediment into porous reservoir rocks (Tissot & Welte, 1978). Since coal is solid and does not migrate, the methylphenanthrene has to come from the oil originating from the coal. The presence of hydrocarbons such as methane in the Basilika formation was also found by Hryniewicz et al. (2016). This suggests that methane and oil were both freely available during ikaite formation. For ikaite to have formed the methane could have then be used as carbon source through anaerobic oxidation of methane into CO_2 and conversion to carbonate (Teichert & Luppold, 2013; Morales et al., 2017).

Petrology and previous ikaite to glendonite transformation mechanisms

In this study a new classification of glendonites was made including three growth generations. The reason why a new classification is made is because type 1a and type 1b look very similar and primarily differ in the amount of inclusions they contain, and have thus been collectively

grouped under 'type 1', while the type 2 generation is different in its occurrence, appearance, and size. The classifications of the different glendonite generations used in this study and other studies are summarized in Table 2 based on their characteristics. Type 1a contains a large abundance of inclusions and does not properly show a texture because it is masked by the inclusions. Type 1b shows more of the crystal texture and contains inclusions in a fibrous appearance (Fig. 5E, 5H, 6A-C). The fibrous texture of this generation is sometimes also found with less or no inclusions (Fig. 6A). Type 1a, 1b are also seen in other petrographic studies, respectively grouped as type 1, type 2 (Huggett et al., 2005; Vickers et al., 2018). Type 2 in this study also has a fibrous texture but differs from type 1 in that it has little to no inclusions. The few inclusions that are visible in this generation are likely part of the overlying type 1 generations, which were cut out when the thin sections were made. This means that the type 2 generation is most likely absent of inclusions. In most of the glendonite samples type 2 is the most ubiquitous generation and often has the largest crystals (e.g. Fig. 5F). The type 2 generation is similar to the yellow calcite and Arc generations seen by Bloem (2019) and genetic phase 3 seen by Morales et al. (2017). Type 2 in this study is often yellow in colour, but, can also occur as white (Fig. 5F). The yellow colour is not unique to the type 2 generation as it has also been identified in the type 1 generations (Fig. 5D, 6B), albeit less often. The studies in Table 2 found different colours for all growth generations, suggesting that the colour of growth generations is likely related to environmental conditions and is thus not a good parameter to define a growth generation. Nevertheless, the colour can be a helpful property to distinguish different growth generations. In Figure 4C of Tollefsen et al. (2020) the glendonite shows a clearly visible fibrous texture with a high porosity. This corresponds best with growth generation type 1b, suggesting this generation is formed during transformation of ikaite to glendonite. Next to the supposed type 1b

Table 2. Summary of glendonite generation classifications

Description	Classification	Authors
White or transparent calcite crystals, oval or irregular in shape. Typically shows little twinning and is often inclusion-rich.	Type 1	Huggett et al. (2005), Vickers et al. (2018), Vickers et al. (2020)
	primary calcite	Greinert & Derkachev (2004)
	Ros (rosettes)	Morales et al. (2017), Bloem (2019)
	replacive calcite	Teichert & Luppold (2013), Qu et al. (2017)
	Type 1a	This study
Fibrous, spherulitic, isopachous, botryoidal, or fibrous to botryoidal calcite rim cement, sometimes containing inclusions	Type 2	Huggett et al. (2005), Vickers et al. (2018), Vickers et al. (2020)
	Rim cement	Greinert & Derkachev (2004), Teichert & Luppold (2013), Qu et al. (2017)
	Rov, Bot	Morales et al. (2017), Bloem (2019)
	Type 1b	This study
Fibrous or anhedral sparry calcite devoid of inclusions	yellow calcite/Arc	Bloem (2019)
	genetic phase 3	Morales et al. (2017)
	Type 2	This study
Clear to anhedral calcite cement acting as filling for pore spaces	Type 3	Huggett et al. (2005), Vickers et al. (2018), Vickers et al. (2020)
	calcite cement	Bloem (2019)
	filling cement	Teichert & Luppold (2013), Qu et al. (2017)
	infilling	This study

generation, small calcite crystals are also formed in the experiment of Tollefsen et al. (2020). A third type of glendonite appearance was not found in the experiment, suggesting it is either only produced in the natural environment, or in a different way, possibly at a later stage. Since the study of Tollefsen et al. (2020) used a laboratory setup it has to be questioned how representative this result is for a naturally transforming ikaite. Nevertheless, since the process of natural ikaite formation is not completely understood and little is known about the transformation to glendonite, the laboratory evidence is important to give an idea about how these processes work. If microscopic imagery of natural ikaite can be obtained the differences between this and synthetic ikaite can be researched.

The Raman spectra (Fig. 8-9) showed that the primary mineral in the glendonites was calcite. No signs of vaterite were found, however, as the background in the Raman spectra was high not many samples were analysed for vaterite, meaning it could have been missed. The lack of vaterite in naturally produced glendonite is supported by all but Ito et al. (1999). In Ito (1998) it is suggested that the vaterite would have been precipitated due to a lack of magnesium in the environment. Magnesium-rich bentonites and clays surround the glendonites in this study. During burial these materials may have exchanged ions such as magnesium with the surrounding water and sediment (Elling et al., 2016), resulting in conditions unfavourable for vaterite formation (Ito, 1998) and thus potentially explaining the lack of vaterite in these glendonites. The broad envelope containing multiple bands in between 1200 and 1500 cm^{-1} is found in all glendonite phases and likely represents organic compounds (Toboła & Botor, 2020). This band was not found in Raman spectra of synthetic glendonite (Sánchez-Pastor et al., 2016). It is unknown what these compounds are and if this signal is trustworthy due to the high background. The high background could have been produced by the oil within the inclusions which could have generated a high amount of fluorescence interfering with the laser. More Raman spectroscopy is warranted on natural glendonites to elucidate the meaning of the broad envelope with multiple bands and also to find if there are other less abundant compounds present in glendonites.

Low temperatures, high phosphate, calcite, and magnesium concentrations, elevated DIC and alkalinity are all factors that contribute to both natural and synthetic ikaite formation (Bischoff et al., 1993; Zabel & Schulz, 2001; Lu et al., 2012; Qu et al., 2017). Ikaite transformation to glendonite is thought to occur in the sulphate-methane transition zone (SMTZ) with a relation to methane (e.g. Zabel & Schulz, 2001; Greinert & Derkachev, 2004; Selleck et al., 2007; Lu et al., 2012; Teichert & Luppold, 2013; Morales et al., 2017) and/or outside this zone without involving methane (e.g. Qu et al., 2017; Vickers et al., 2018). The hypothesis of ikaite to glendonite transformation in the SMTZ is largely based on carbon isotope data, sulphide isotope data, and biomarker data. With this in mind and considering the petrology of glendonites, different transformation mechanisms have been proposed to describe the change from ikaite to glendonite.

The model from Greinert & Derkachev (2004) describes the change from ikaite to glendonite to be induced by the movement of the SMTZ to the seafloor surface, which would cause leaking of sulphate into the water and thus less sulphate reduction in the sediment. A decrease in sulphate reduction leads to a decrease in the organic matter decomposition rate, which would decrease the release of phosphate and HCO_3^- in the sediment. Since phosphate inhibits the formation of other calcium carbonate phases than ikaite (Bischoff et al., 1993), a decrease in the phosphate concentration will lead to less ikaite being deposited and more other calcium carbonate phases, thus destabilizing ikaite. The decrease in alkalinity also results in less calcium carbonate being precipitated, further reducing ikaite formation. According to Greinert & Derkachev (2004) the destabilization of ikaite triggers the transformation of ikaite to calcite, or glendonite. They propose that two forms of calcite forms in this transformation mechanism. The first form is pseudomorph calcite which replaced the original ikaite crystal. The second form is high-Mg calcite which is precipitated in the pore spaces of the glendonite, which are formed during transformation from

ikaite to glendonite at the places where water was previously located. The Mg-calcite is also thought to have been precipitated in the sediment. The Mg-calcite from Greinert & Derkachev (2004) is described as euhedral, which could be related to either type 1b without inclusions (Fig. 6A) or type 2 (Fig. 6C) from this study, both without the fibrous character. The Raman shift of calcite increases linearly with increasing substitution of calcite ions by magnesium ions (Borromeo et al., 2017). The glendonite generations in this study showed a Raman shift close to 1086 cm^{-1} , suggesting that it is calcite with little magnesium incorporated in its structure (Borromeo et al., 2017). Therefore, the presence of high-Mg calcite was not found in this study. This model further proposes that high sulphate reduction rates at the SMTZ can induce in-situ pyrite deposition and enhances pyrite deposition at the iron-sulphate transition zone through increased migration of H_2S , produced at the SMTZ. The first scenario can occur when iron is available in the SMTZ in close proximity to AOM and sulphate reduction, which can then reduce to pyrite (Peckmann & Thiel, 2004). The second scenario is the effect of AOM coupled to sulphate reduction when the sediment is porous enough for fluid migration to occur. This model would explain the high amount of pyrite as seen in this study (Fig. 5A). In this model it is not explained why the glendonite generations have a certain morphology. In conclusion, with different morphologies found by Greinert & Derkachev (2004) compared to this study, different calcite types found, and the lack of explanation on the morphologies, this transformation model is difficult to apply to the glendonites in this study.

Vickers et al. (2018) created two models of ikaite transformation to glendonite, mainly differing from each other in the speed of transformation and the degree of textural zoning. The first of their models describes a rapid breakdown of ikaite into unzoned glendonite where type 1a zoned grains containing inclusions are formed by solid-state transformation of ikaite to vaterite, which quickly reprecipitates as calcite. In this model they assume that vaterite is formed as intermediate phase (e.g. Ito, 1998; Tang et al. 2009). Type 1b in this model is seen as an overgrowth of type 1a precipitated from porewaters coming from the sediments and from conversion of the rest of the ikaite crystal to calcite. The overgrowth of type 1b is also seen in this study in Fig. 5G-I and Fig. 6A. They consider the growth of both these generations to happen inside the sulphate reduction zone until the glendonite moves out of this zone. Outside the sulphate reduction zone calcite precipitation is thought to become unfavourable as seen by etched boundaries on their type 2. These etched boundaries are not found on type 1b in this study. The type 2 calcite in this study is thought to have formed at a later point in time. In this study later infilling of voids in the glendonite has also been identified, but here they are indicated as IF (infilling) and found in little amounts (e.g. Fig. 5H-I, 6E, 6G). The infilling found in this study is not similar to that of what Vickers et al. (2018) considers infilling in their type 3 but is similar to the calcite cement of Bloem (2019). Other studies identified carbonate infilling as type 2 (e.g. Huggett et al., 2005; Teichert & Luppold, 2013). In these studies the term 'infilling' is treated as an observation, while the type 2 in this study is not observed as simple infilling. The observed infilling in this study is thus not called type 2, but instead called 'IF'. Other than the difference in interpretation of type 2 being infilling, the type 2 of this study and type 3 of Huggett et al. (2005) and Vickers et al. (2018) are very similar. In this study the type 2 generation is rarely observed as having been diagenetically altered after formation, but when found, it is observed as twinned crystals in the shape of the fibrous texture (Fig. 5Q). Type 2 often makes up the outer generation of the glendonite bordering the sediment around (Fig. 5B-C). This is in line with the rapid destabilisation model of Vickers et al. (2018), which suggest that this generation is mainly found at the outside of the crystals. The second model describes a slow, progressive breakdown of ikaite to macro-zoned glendonite. This model regards this breakdown as happening from the outside of the ikaite crystal towards the inside. They hypothesize that these ikaites oscillate around the ikaite stability field, destabilizing the outer edge of the ikaite crystal and in a slow rate also the inner part of the crystal. Tollefsen et al. (2020) found the slow breakdown model of Vickers et al. (2018) to

correspond to most of their results, but also found the rapid breakdown fitting for some results. Teichert & Luppold (2013) also concluded from their results that the inner crystal of the ikaite remains stable for a longer time, as opposed to the margins. The petrology of the Basilika Formation glendonites seems to be more in line with that of the rapid destabilisation model of Vickers et al. (2018) as the glendonites do not seem to show signs of macro-zoning. These models do not go in depth about how these inclusions were formed. In the following section this is incorporated.

Formation of inclusions and implications for transformation mechanisms

From the inclusion images (Fig. 7) the black and brown colours in Fig. 7A-B suggest the presence of a fluid inside these inclusions. These inclusions are viewed as oval bubbles or droplets, where the black colour are likely caused by Becke lines, which are bright or dark lines created by diffraction and/or refraction of light, and which form at the boundary between different media with different optical path lengths (Davidson & Florida State University, 2015). The Becke lines change with the focus of the microscope (Davidson & Florida State University, 2015). When viewed out-of-focus (Fig. 7A), the brown colour appearing is very reminiscent of oil. This suggests that the insides of the inclusions may contain fluids such as oil and water and are thus not empty. The oil would have come from the coal layers in the Firkanten formation and migrated into the Basilika formation. The oil and water could have been accompanied by impurities such as methane. When zoomed-in, the inside of this bubble or droplet becomes transparent and only the edges are black (Fig. 7C). This is probably the effect of the Becke lines brightening the colours inside and darkening the colours on the edges, thus shading the brown colour. That inclusions are filled has been proposed before by Morales et al. (2017) and den Boer (2019) who measured hydrocarbon gases such as methane from glendonite inclusions. They also found the methane to be of thermogenic origin, where den Boer (2019) specifically interpreted it as coming from the thermogenic cracking of oil. Methane could have travelled together with oil for the glendonites in this study, although there was no observation of methane in the Raman or biomarker data. As ikaite is often euhedral without cavities and glendonite is porous (Tollefsen et al., 2020), the inclusions are likely only present in the glendonites and not in the ikaite. This is supported by Kodina et al., (2003) who found small white inclusions in ikaite crystals formed during ikaite transformation to glendonite. The oil migrating through the sediment probably filled these inclusions during ikaite transformation to glendonite, leading to the brown colours. A possible mechanism for this is that during ikaite transformation the water released from the structure contained oil bubbles or droplets on which glendonite precipitated. Calcium carbonate nucleation can occur at the surfaces of microbubbles (Fatemi et al., 2019), and is enhanced at water droplets containing impurities (Zhang et al., 2020). If no solid-state transformation from ikaite to glendonite is assumed, the glendonites will precipitate from water containing impurities such as oil. The (micro)bubbles or droplets of oil can then act as surfaces for glendonite precipitation. This is supported by Tzachristas et al. (2021) who found calcium carbonate nucleation to be enhanced at oil/water interfaces. The oil could have intruded from outside the ikaite during release of water from the ikaite structure during transformation, resulting in bubbles or droplets, or it could have been incorporated in the ikaite structure from the start as impurity and then released together with the water (Fig. 14). It is unknown which of the two is the case and this could possibly be elucidated by analysing the composition of natural ikaite grown in a depositional environment where oil migration occurs. In this mechanism the ikaite crystals are assumed to have been largely dissolved to allow fluids with different quantities of microbubbles to enter before reprecipitating as glendonite around these bubbles. The type 1a generation contains more inclusions than the type 1b generation. Type 1a is then expected to have had more oil/water interfaces than type 1b. With more oil/water interfaces

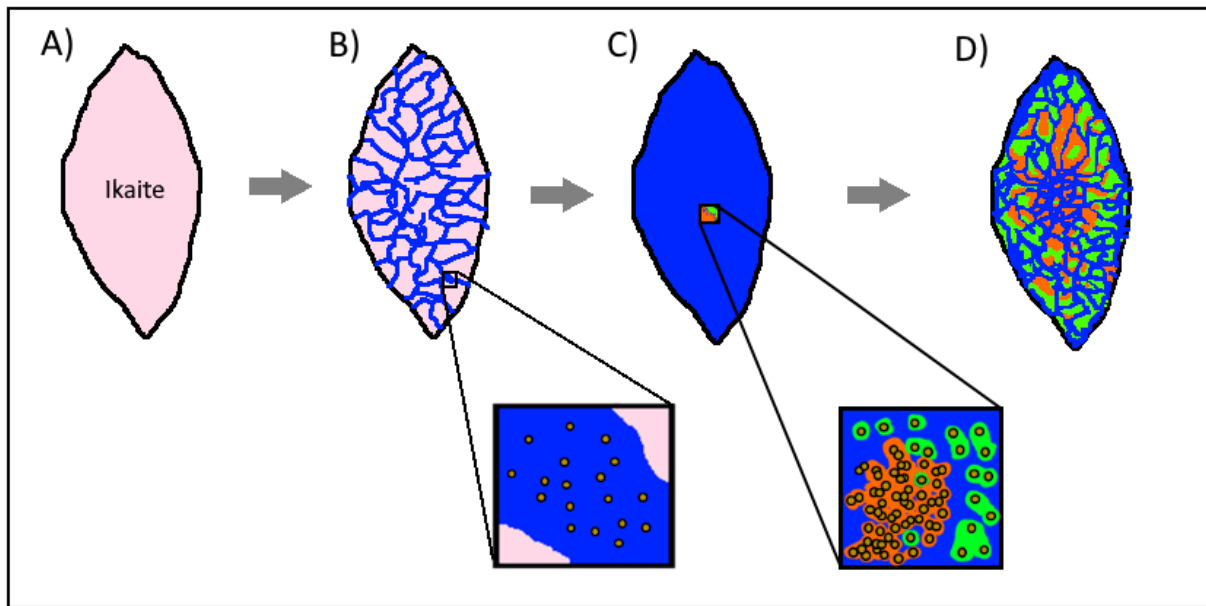


Figure 14. Schematic figure of the mechanism of crystal nucleation at oil/water-interfaces mediated by the water released from the ikaite structure. The ikaite crystal (A) destabilises and the water from the ikaite structure becomes freely available (B). This water contains oil bubbles (brown circles) which were stuck as impurities in the ikaite and were released along with the water. The ikaite largely dissolves and reprecipitates around the oil bubbles where the type 1a generation (orange colour) is precipitated around clusters of bubbles, and the type 1b generation (green colour) is precipitated at places of low bubble density (C). Once all ikaite has been reprecipitated no more type 1a and type 1b will be formed (D).

the calcium carbonate nucleation will be accelerated but the individual crystal growth rate will be decreased (Tzachristas et al., 2021). This suggests that type 1a was precipitated at a faster pace than type 1b, but once precipitated, the individual crystals grew at a slower rate for type 1a than for type 1b. If both generations grew for the same period of time, type 1a with more inclusions will show less crystal texture than type 1b, which has a lower amount of inclusions. Since the type 1a in this study has a smaller amount of crystal texture and is more filled with inclusions, the growth time of type 1a and type 1b is expected to be similar, or type 1b grew for longer than type 1a. However, growth rate of these generations has not been measured in this study or previously in the literature, so this statement has to be considered very carefully. The lack of inclusions in the type 2 generation suggests that this was not formed through calcium carbonate nucleation around bubbles/droplets. If the type 2 generation is simply calcium carbonate precipitated from solution due to oversaturation of calcium carbonate, then this would have been deposited after the type 1 generations, as calcium carbonate nucleation is faster at oil/water interfaces and around microbubbles (Fatemi et al., 2019, Zhang et al., 2020, Tzachristas et al., 2021). Supporting this is that type 1a and type 1b generations are often surrounded by the type 2 generation (Fig. 5E, 5G-I, 6C, 6F) and type 2 is often forming the outside generation of the glendonites (Fig. 5B-C, 6H). The white rim around the inclusions (Fig. 7) is slightly distinguishable in the Raman spectra as a yellow-white band around the inclusions (Fig. 8B), indicating it contains some calcite. It is unclear what these white rims exactly are, how they are formed, or why they are present around inclusions. Further research on inclusions in glendonites is necessary to find out if there is a relation with the composition of inclusions and glendonite formation and why these inclusions have this particular morphology.

The transformation mechanism of Greinert & Derkachev (2004) does not discuss inclusions, while the rapid destabilisation model from Vickers et al. (2018) only noted their presence. In the rapid destabilisation model the inclusions are thought to have formed during ikaite transformation to glendonite. This is in line with the interpretation from this study. In Vickers et al. (2018) vaterite is thought to have formed by solid-state transformation of ikaite during ikaite destabilisation. The

vaterite would then quickly dissolve in the water and reprecipitate as calcite to form the type 1a generation. They suggest that the type 1b generation is precipitated as calcite over the type 1a generation. They interpreted the type 2 generation as having been deposited at a later point in time as diagenetic sparry calcite to fill the remaining voids in the glendonite. Because of the similarity in looks and the presence of inclusions in the type 1a and type 1b generations, the difference between the two generations could merely be the amount of inclusions, and do not have to require a different fluid source. No vaterite was found in glendonites and no natural vaterite in ikaite has been found in magnesium-rich environments to date, leaving only lab results of vaterite derived from synthetic ikaite to serve as evidence for vaterite to be formed as an intermediate product in these environments. It is not known whether the lab evidence is representative or not. Furthermore, the type 1a generation is inclusion-rich while dissolution-recrystallization of vaterite into calcite is shown to form a dense calcite structure with no voids (Cherkas et al., 2018). Neither is it expected for inclusions to form during a solid-state transformation from ikaite to vaterite as solid-state transformations preserve the morphology and crystallographic relationships between the parent phase and product (Ruiz-Agudo et al., 2014). Since ikaite is thought to be euhedral without pores (Tollefsen et al., 2020), vaterite would then show a similar appearance. If vaterite is not considered as an intermediate product, these generations are probably both formed as a mix of water from the ikaite structure and calcium carbonate from dissolved ikaite, through a normal dissolution-reprecipitation mechanism.

An alternative mechanism for the formation of inclusions could involve coupled dissolution and precipitation at mineral-fluid interfaces between ikaite and the fluid released during destabilisation (Ruiz-Agudo et al., 2014). In this mechanism some dissolution at the interface of ikaite crystals is induced by an aqueous fluid, interpreted to be the water extruded from the ikaite structure during destabilisation of the ikaite mineral. This leads to a supersaturated boundary layer with respect to one or more phases of calcium carbonate. One of the stable calcium carbonate phases will then reprecipitate on the ikaite phase as a porous phase. This porosity allows the inner crystal to remain in contact with the water, allowing the same reaction to occur (Fig. 15). This

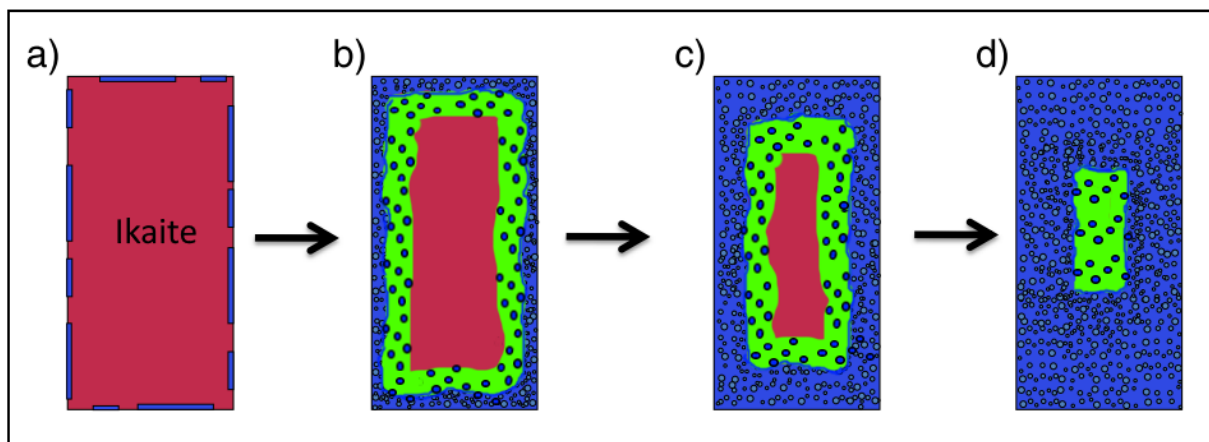


Figure 15. Schematic figure of the mineral-interface coupled dissolution-precipitation mechanism from the outside propagating inward (a-d). The green colour represents the type 1b calcite with few inclusions, the blue colour represents the type 1a colour and contains many inclusions, and the pink colour represents the original ikaite. This process is incomplete as there is some type 1b present in (d). Modified from Ruiz-Agudo et al., 2014.

reaction happens at a very fast rate (Ruiz-Agudo et al., 2014). In this mechanism vaterite could possibly be considered as an intermediate, but the rate of vaterite dissolution and reprecipitation is much slower than is proposed for this mechanism (Cherkas et al., 2018). If this mechanism occurs from the outside of a mineral towards the inside, the inner parts of the mineral could be less porous if the mechanism is incomplete (Fig. 15d). This could explain the formation of type 1a, a generation

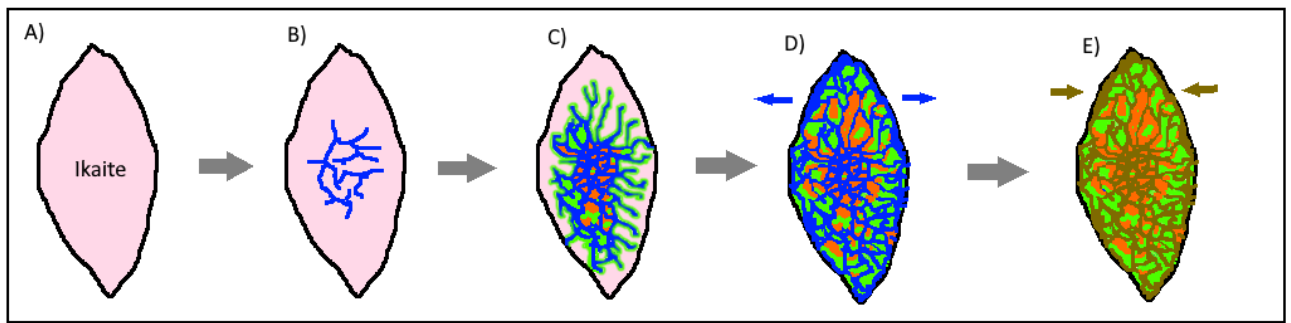


Figure 16. Schematic figure of the mineral-interface coupled dissolution-precipitation mechanism from inside propagating outward. The stable ikaite (A) becomes unstable and releases the water in its crystal structure (blue colour) starting from the inside (B), propagating outward. The water will cause dissolution of the ikaite and precipitation of porous calcite, initially with few inclusions (type 1b, green colour), but rapidly forming many inclusions (type 1a, orange colour) from the outside of an ikaite fragment towards the inside. The whole ikaite becomes unstable and water leaves the crystal (D). During this step more type 1a and type 1b generations are formed. The water is quickly replaced by pore waters from the sediment, depositing the type 2 generation (brown colour, E). Inclusions are not drawn in this figure.

with many inclusions, and type 1b, a generation with fewer inclusions. Tollefsen et al. (2020) found that synthetic ikaite is replaced both from inside outward and outside inward. If the water released from the ikaite structure during destabilisation of the mineral induces mineral-fluid interface dissolution-precipitation, then dissolution and precipitation could occur throughout the whole ikaite as long as there is a mineral-fluid interface present. If this mechanism works from inside outward and is not completed, the inside would consist of many inclusions, while the outside would contain fewer inclusions. Since type 1b is usually surrounding type 1a it means that the inner generation is usually more porous than the outside. Therefore, it would make more sense for the mineral-interface coupled dissolution-precipitation to start from inside the ikaite crystal and work towards the outside and then stop before the outside part of the crystal is as porous as the inside (Fig. 16). Furthermore, the Fig. 15 model where dissolution-precipitation occurs from the outside inward also lacks the occurrence of water leaving the ikaite structure and the precipitation of type 2 calcite. This suggests that the mechanism as described in Fig. 15 is unlikely. In the scenario where dissolution-precipitation happens from the inside out the mediating fluid would have to be the water from the ikaite structure. Nothing points to the requirement of oil for this mechanism to take place, but there could have been oil impurities inside the ikaite structure which would have entered the inclusions during dissolution and precipitation.

The difference between the mineral-interface coupled dissolution-precipitation mechanism and the mechanism of crystal nucleation at oil/water-interfaces is that the former considers the ikaite to be destabilised from the inside outward, where the mediating fluid is the water from the ikaite structure, while in the latter it is not clear if the mediating fluid is the water from inside the ikaite structure or pore water from the sediments. In the mechanism of crystal nucleation at oil/water-interfaces the occurrence of type 2 is not explained, but if the mechanism uses the water from the ikaite structure to form the type 1 generations, the type 2 generation could have been produced by intruding fluids from the sediment, as is proposed for the mineral-interface coupled dissolution-precipitation mechanism. To find which mechanism is more likely to occur nano-imaging methods can be performed on synthetic ikaite to observe the dissolution and precipitation mechanism when transforming into glendonite.

Conclusion

Glendonites and surrounding sediments from the Basilika Formation of Spitsbergen show signs of containing oil. In the glendonites this oil is likely present in the inclusions, mixed with water and potentially hydrocarbon gases. Raman spectroscopy shows that the calcium carbonate phase of glendonites is calcite and shows no sign of vaterite. From the petrology it can be seen that the growth generations type 1a and type 1b look very similar and it is hypothesized in this study that these generations are both produced by a mix of ikaite calcium carbonate and water containing oil and hydrocarbon gases inside the ikaite structure. The type 2 generation shows little to no inclusions and is interpreted to have been formed in a different manner than the type 1 generations. Two fluid mediated crystal nucleation mechanisms producing inclusion-bearing glendonite generations have been proposed, one where these generations are formed through crystal nucleation on oil bubbles or droplets, and one where the generations are formed through coupled dissolution and precipitation at ikaite-water interfaces. The former mechanism suggests that the presence of oil facilitates glendonite formation, while the latter does not seem to have a relationship with oil. More research on inclusions in glendonites is necessary to confirm the relationship between oil and glendonite formation.

References

- Aquilina, A., Knab, N. J., Knittel, K., Kaur, G., Geissler, A., Kelly, S. P., Fossing, H., Boot, C. S., Parkes, R. J., Mills, R. A., Boetius, A., Lloyd, J. R., & Pancost, R. D. (2010). Biomarker indicators for anaerobic oxidizers of methane in brackish-marine sediments with diffusive methane fluxes. *Organic Geochemistry*, *41*(4), 414–426. <https://doi.org/10.1016/j.orggeochem.2009.09.009>
- Bian, L., Hinrichs, K. U., Xie, T., Brassell, S. C., Iversen, N., Fossing, H., Jørgensen, B. B., & Hayes, J. M. (2001). Algal and archaeal polyisoprenoids in a recent marine sediment: Molecular isotopic evidence for anaerobic oxidation of methane. *Geochemistry, Geophysics, Geosystems*, *2*(1). <https://doi.org/10.1029/2000GC000112>
- Bischoff, J. L., Fitzpatrick, J. A., & Rosenbauer, R. J. (1993). The solubility and stabilization of ikaite (CaCO₃·6H₂O) from 0° to 25°C: environmental and paleoclimatic implications for thynolite tufa. *Journal of Geology*, *101*(1), 21–33. <https://doi.org/10.1086/648194>
- Bloem, M. (2019). *The Petrology and Inorganic Geochemistry of Glendonites: Insights into the enigmatic ikaite-to-glendonite transformation using a detailed combinative approach*. [Unpublished manuscript]. Department of Earth Sciences, Utrecht University.
- Blumenberg, M., Seifert, R., Reichart, G.J., Pape, T., Michaelis, W., 2004. Membrane lipid patterns typify distinct anaerobic methanotrophic consortia. *Proc. Natl. Acad. Sci.* *101*, 11111–11116. <https://doi.org/10.1073/pnas.0401188101>
- Blumenberg, M., Pape, T., Seifert, R., Bohrmann, G., & Schlömer, S. (2018). Can hydrocarbons entrapped in seep carbonates serve as gas geochemistry recorder? *Geo-Marine Letters*, *38*(2), 121–129. <https://doi.org/10.1007/s00367-017-0522-6>
- Blumer, M., Mullin, M. M., & Thomas, D. W. (1963). Pristane in Zooplankton. *Science*, *140*(3570), 974–974. <https://doi.org/10.1126/science.140.3570.974.a>

- Boer, M. Den. (2019). *The link between methane seepage and glendonites: An insight from gas inclusions and biomarkers* [Unpublished manuscript]. Department of Earth Sciences, Utrecht University.
- Boehm, P. D. (2005). Polycyclic Aromatic Hydrocarbons (PAHs). *Environmental Forensics: Contaminant Specific Guide*, 313–337. <https://doi.org/10.1016/B978-012507751-4/50037-9>
- Borromeo, L., Zimmermann, U., Andò, S., Coletti, G., Bersani, D., Basso, D., Gentile, P., Schulz, B., & Garzanti, E. (2017). Raman spectroscopy as a tool for magnesium estimation in Mg-calcite. *Journal of Raman Spectroscopy*, 48(7), 983–992. <https://doi.org/10.1002/jrs.5156>
- Bray, E. E., & Evans, E. D. (1961). Distribution of n-paraffins as a clue to recognition of source beds. *Geochimica et Cosmochimica Acta*, 22(1), 2–15. [https://doi.org/10.1016/0016-7037\(61\)90069-2](https://doi.org/10.1016/0016-7037(61)90069-2)
- Brooks, J. D., Gould, K., & Smith, J. W. (1969). Isoprenoid hydrocarbons in coal and petroleum. *Nature*, 222(5190), 257–259. <https://doi.org/10.1038/222257a0>
- Cherkas, O., Beuvier, T., Zontone, F., Chushkin, Y., Demoulin, L., Rousseau, A., & Gibaud, A. (2018). On the kinetics of phase transformations of dried porous vaterite particles immersed in deionized and tap water. *Advanced Powder Technology*, 29(11), 2872–2880. <https://doi.org/10.1016/j.apt.2018.08.008>
- Dallmann, W. K. (1999). *Lithostratigraphic Lexicon of Svalbard*. Tromsø: Norsk Polarinstitut.
- Davidson, W. M., & Florida State University, “Friedrich Johann Karl Becke”, last modified 13 Nov 2015, <https://micro.magnet.fsu.edu/optics/timeline/people/becke.html>
- DeCarlo, T. M. (2018). Characterizing coral skeleton mineralogy with Raman spectroscopy. *Nature Communications*, 9(1), 9–11. <https://doi.org/10.1038/s41467-018-07601-3>
- Dypvik, H., & Nagy, J. (1978). Early Tertiary Bentonites from Svalbard; a Preliminary Report. *Polarforschung*, 48(1/2), 139–150.
- Elling, F. J., Spiegel, C., Estrada, S., Davis, D. W., Reinhardt, L., Henjes-Kunst, F., Allroggen, N., Dohrmann, R., Piepjohn, K., & Lisker, F. (2016). Origin of bentonites and detrital zircons of the Paleocene Basilika formation, Svalbard. *Frontiers in Earth Science*, 4(July). <https://doi.org/10.3389/feart.2016.00073>
- Elvert, M., Suess, E., Greinert, J., & Whiticar, M. J. (2000). Archaea mediating anaerobic methane oxidation in deep-sea sediments at cold seeps of the eastern Aleutian subduction zone. *Organic Geochemistry*, 31(11), 1175–1187. [https://doi.org/10.1016/S0146-6380\(00\)00111-X](https://doi.org/10.1016/S0146-6380(00)00111-X)
- Fatemi, N., Dong, Z., Van Gerven, T., & Kuhn, S. (2019). Microbubbles as Heterogeneous Nucleation Sites for Crystallization in Continuous Microfluidic Devices. *Langmuir*, 35(1), 60–69. <https://doi.org/10.1021/acs.langmuir.8b03183>
- Greinert, J., & Derkachev, A. (2004). Glendonites and methane-derived Mg-calcites in the Sea of Okhotsk, Eastern Siberia: Implications of a venting-related ikaite/glendonite formation. *Marine Geology*, 204(1–2), 129–144. [https://doi.org/10.1016/S0025-3227\(03\)00354-2](https://doi.org/10.1016/S0025-3227(03)00354-2)
- Herrera-Herrera, A. V., Leierer, L., Jambriña-Enríquez, M., Connolly, R., & Mallof, C. (2020). Evaluating different methods for calculating the Carbon Preference Index (CPI): Implications for

palaeoecological and archaeological research. *Organic Geochemistry*, 146, 104056. <https://doi.org/10.1016/j.orggeochem.2020.104056>

- Hryniewicz, K., Bitner, M. A., Durska, E., Hagström, J., Hjálmsdóttir, H. R., Jenkins, R. G., Little, C. T. S., Miyajima, Y., Nakrem, H. A., & Kaim, A. (2016). Paleocene methane seep and wood-fall marine environments from Spitsbergen, Svalbard. *Palaeogeography, Palaeoclimatology, Palaeoecology*, 462, 41–56. <https://doi.org/10.1016/j.palaeo.2016.08.037>
- Huang, S. Y., Li, M. J., Zhang, K., Wang, T. G., Xiao, Z. Y., Fang, R. H., Zhang, B. S., Wang, D. W., Zhao, Q., & Yang, F. L. (2016). Distribution and geochemical significance of phenylphenanthrenes and their isomers in selected oils and rock extracts from the Tarim Basin, NW China. *Petroleum Science*, 13(2), 183–191. <https://doi.org/10.1007/s12182-016-0095-4>
- Huggett, J. M., Schultz, B. P., Shearman, D. J., & Smith, A. J. (2005). The petrology of ikaite pseudomorphs and their diagenesis. *Proceedings of the Geologists' Association*, 116(3–4), 207–220. [https://doi.org/10.1016/S0016-7878\(05\)80042-2](https://doi.org/10.1016/S0016-7878(05)80042-2)
- Ito, T. (1998). Factors controlling the transformation of natural ikaite from Shiowakka, Japan. *Geochemical Journal*, 32(4), 267–273. <https://doi.org/10.2343/geochemj.32.267>
- Ito, T., Matsubara, S., & Miyawaki, R. (1999). Vaterite after ikaite in carbonate sediment. In *Journal of Mineralogy, Petrology and Economic Geology* (Vol. 94, Issue 5, pp. 176–182). <https://doi.org/10.2465/ganko.94.176>
- Johns, R. ., Belsky, T., McCarthy, E. ., Burlingame, A. ., Haug, P., Schnoes, H. ., Richter, W., & Calvin, M. (1966). The organic geochemistry of ancient sediments—Part II. *Geochimica et Cosmochimica Acta*, 30(12), 1191–1222. [https://doi.org/10.1016/0016-7037\(66\)90120-7](https://doi.org/10.1016/0016-7037(66)90120-7)
- Kodina, L.A., Tokarev, V.G., Vlasova, L.N., Korobeinik, G.S., 2003. Contribution of biogenic methane to ikaite formation in the Kara Sea: evidence from the stable carbon isotope geochemistry. In: Stein, R., et al. (Ed.), Siverian river run-off in the Kara Sea, Proc. in Marine Sciences, vol. 6. Elsevier, Amsterdam, pp. 349–374
- Larsen, D. (1994). Origin and Paleoenvironmental Significance of Calcite Pseudomorphs after Ikaite in the Oligocene Creede Formation, Colorado. *SEPM Journal of Sedimentary Research*, Vol. 64A. <https://doi.org/10.1306/D4267E1A-2B26-11D7-8648000102C1865D>
- Lu, Z., Rickaby, R. E. M., Kennedy, H., Kennedy, P., Pancost, R. D., Shaw, S., Lennie, A., Wellner, J., & Anderson, J. B. (2012). An ikaite record of late Holocene climate at the Antarctic Peninsula. *Earth and Planetary Science Letters*, 325–326, 108–115. <https://doi.org/10.1016/j.epsl.2012.01.036>
- Maher, H. D. (2001). Manifestations of the Cretaceous High Arctic Large Igneous Province in Svalbard. *The Journal of Geology*, 109(1), 91–104. <https://doi.org/https://doi.org/10.1086/317960>
- Major, H., and Nagy, J. (1972). Geology of the Adventdalen Map Area. (Tromsø: Norsk Polarinstittutt), 138.
- Mangin, D., Puel, F., & Veessler, S. (2009). Polymorphism in processes of crystallization in solution: A practical review. *Organic Process Research and Development*, 13(6), 1241–1253. <https://doi.org/10.1021/op900168f>

- Marland, G. (1975). The stability of $\text{CaCO}_3 \cdot 6\text{H}_2\text{O}$ (ikaite). *Geochimica et Cosmochimica Acta*, 39(1), 83–91. [https://doi.org/10.1016/0016-7037\(75\)90186-6](https://doi.org/10.1016/0016-7037(75)90186-6)
- Marzi, R., Torkelson, B. E., & Olson, R. K. (1993). A revised carbon preference index. *Organic Geochemistry*, 20(8), 1303–1306. [https://doi.org/10.1016/0146-6380\(93\)90016-5](https://doi.org/10.1016/0146-6380(93)90016-5)
- Mello, M., Koutsoukos, E., Hart, M. B., & Brassell, S. (1989). *Late Cretaceous anoxic events in the Brazilian continental margin*. *Late Cretaceous anoxic events in the Brazilian continental margin*. 6380(December). [https://doi.org/10.1016/0146-6380\(89\)90033-8](https://doi.org/10.1016/0146-6380(89)90033-8)
- Micera, M., Botto, A., Geddo, F., Antoniotti, S., Berteà, C. M., Levi, R., Gallo, M. P., & Querio, G. (2020). Squalene: More than a step toward sterols. *Antioxidants*, 9(8), 1–14. <https://doi.org/10.3390/antiox9080688>
- Morales, C., Rogov, M., Wierzbowski, H., Ershova, V., Suan, G., Adatte, T., Föllmi, K. B., Tegelaar, E., Reichart, G. J., de Lange, G. J., Middelburg, J. J., & van de Schootbrugge, B. (2017). Glendonites track methane seepage in Mesozoic polar seas. *Geology*, 45(6), 503–506. <https://doi.org/10.1130/G38967.1>
- Müller, R. D., & Spielhagen, R. F. (1990). Evolution of the Central Tertiary Basin of Spitsbergen : towards a synthesis of sediment and plate tectonic history. *Palaeogeography, Palaeoclimatology, Palaeoecology*, 80(2), 153–172.
- Nagy, J. E. N. Ö., Kaminski, M. A., & Kuhnt, W. (2000). *Agglutinated Foraminifera from Neritic to Bathyal Facies in the Palaeogene of Spitsbergen and the Barents Sea*. 333–361.
- Nissenbaum, A., Baedeker, M. J., & Kaplan, I. R. (1972). Organic geochemistry of Dead Sea sediments. *Geochimica et Cosmochimica Acta*, 36(7), 709–727. [https://doi.org/10.1016/0016-7037\(72\)90082-8](https://doi.org/10.1016/0016-7037(72)90082-8)
- Noble, R., Alexander, R., & Kagi, R. I. (1985). The occurrence of bisnorhopane, trisnorhopane and 25-norhopanes as free hydrocarbons in some Australian shales. *Organic Geochemistry*, 8(2), 171–176. [https://doi.org/10.1016/0146-6380\(85\)90035-X](https://doi.org/10.1016/0146-6380(85)90035-X)
- Pancost, R.D., Hopmans, E.C., Sinnighe Damste, J.S., Party, T.M.S.S., 2001. Archaeal lipids in Mediterranean cold seeps: molecular proxies for anaerobic methane oxidation. *Geochim. Cosmochim. Acta* 65, 1611–1627.
- Pauly, H. (1963). “Ikaite”, a New Mineral from Greenland. *Arctic*, 16(4), 263. <https://doi.org/10.14430/arctic3545>
- Peckmann, J., & Thiel, V. (2004). Carbon cycling at ancient methane-seeps. *Chemical Geology*, 205(3–4), 443–467. <https://doi.org/10.1016/j.chemgeo.2003.12.025>
- Peters, K. E., Walters, C. C., & Moldowan, J. M. (2004). Source- and age-related biomarker parameters. In *The Biomarker Guide*. <https://doi.org/10.1017/cbo9781107326040.004>
- Pi, Y., Ye, Q., Jiang, H., Wang, P., Li, S., Noakes, J., Culp, R., Dong, H., Zhang, C., Pi, Y., Ye, Q., Jiang, H., Wang, P., Li, S., Noakes, J., Culp, R., Dong, H., & Zhang, C. (2009). Archaeal Lipids and 16S rRNA Genes Characterizing Non-hydrate and Hydrate-Impacted Sediments in the Gulf of Mexico. *Geomicrobiology Journal* 0451(May). <https://doi.org/10.1080/01490450902889411>

- Powell, T. G., & McKirdy, D. M. (1973). Relationship between Ratio of Pristane to Phytane, Crude Oil Composition and Geological Environment in Australia. *Nature Physical Science*, 243(124), 37–39. <https://doi.org/10.1038/physci243037a0>
- Qu, Y., Teichert, B. M. A., Birgel, D., Goedert, J. L., & Peckmann, J. (2017). The prominent role of bacterial sulfate reduction in the formation of glendonite: a case study from Paleogene marine strata of western Washington State. *Facies*, 63(2). <https://doi.org/10.1007/s10347-017-0492-1>
- Ruiz-Agudo, E., Putnis, C. V., & Putnis, A. (2014). Coupled dissolution and precipitation at mineral-fluid interfaces. *Chemical Geology*, 383, 132–146. <https://doi.org/10.1016/j.chemgeo.2014.06.007>
- Rullkötter, J., & Wendisch, D. (1982). Microbial alteration of 17 α (H)-hopanes in Madagascar asphalts: removal of C-10 methyl group and ring opening. *Geochimica et Cosmochimica Acta*, 46(9), 1545–1553. [https://doi.org/10.1016/0016-7037\(82\)90313-1](https://doi.org/10.1016/0016-7037(82)90313-1)
- Sánchez-Pastor, N., Oehlerich, M., Astilleros, J. M., Kaliwoda, M., Mayr, C. C., Fernández-Díaz, L., & Schmahl, W. W. (2016). Crystallization of ikaite and its pseudomorphic transformation into calcite: Raman spectroscopy evidence. *Geochimica et Cosmochimica Acta*, 175, 271–281. <https://doi.org/10.1016/j.gca.2015.12.006>
- Savard, M. M., Beauchamp, B., & Veizer, J. (1996). Significance of Aragonite Cements Around Cretaceous Marine Methane Seeps. *SEPM Journal of Sedimentary Research*, Vol. 66. <https://doi.org/10.1306/D4268365-2B26-11D7-8648000102C1865D>
- Selleck, B. W., Carr, P. F., & Jones, B. G. (2007). A review and synthesis of glendonites (pseudomorphs after ikaite) with new data: Assessing applicability as recorders of ancient coldwater conditions. *Journal of Sedimentary Research*, 77(11–12), 980–991. <https://doi.org/10.2110/jsr.2007.087>
- Shearman, D. J., & Smith, A. J. (1985). Ikaite, the parent mineral of jarrowite-type pseudomorphs. *Proceedings of the Geologists' Association*, 96(4), 305–314. [https://doi.org/10.1016/S0016-7878\(85\)80019-5](https://doi.org/10.1016/S0016-7878(85)80019-5)
- Spielhagen, R. F., & Tripathi, A. (2009). Evidence from Svalbard for near-freezing temperatures and climate oscillations in the Arctic during the Paleocene and Eocene. *Palaeogeography, Palaeoclimatology, Palaeoecology*, 278(1–4), 48–56. <https://doi.org/10.1016/j.palaeo.2009.04.012>
- Steel, R. J., Dalland, A., Kalgraff, K., & Larsen, V. (1981). The Central Tertiary Basin of Spitsbergen: Sedimentary Development of a Sheared-Margin Basin. *Geology of the North Atlantic Borderlands*, 7(1981), 647–664.
- Stockmann, G. J., Ranta, E., Trampe, E., Sturkell, E., & Seaman, P. (2018). Carbon mineral storage in seawater: Ikaite (CaCO₃ · 6H₂O) columns in Greenland. *Energy Procedia*, 146, 59–67. <https://doi.org/10.1016/j.egypro.2018.07.009>
- Suess, E., Balzer, W., Hesse, K.-F., Müller, P. J., Ungerer, C. A., & Wefer, G. (1982). Calcium Carbonate Hexahydrate from Organic-Rich Sediments of the Antarctic Shelf: Precursors of Glendonites. *Science*, 216(4550), 1128–1131. <https://doi.org/10.1126/science.216.4550.1128>
- Swainson, I. P., & Hammond, R. P. (2001). Ikaite, CaCO₃ · 6H₂O: Cold comfort for glendonites as paleothermometers. *American Mineralogist*, 86(11–12), 1530–1533. <https://doi.org/10.2138/am-2001-11-1223>

- Tang, C. C., Thompson, S. P., Parker, J. E., Lennie, A. R., Azough, F., & Kato, K. (2009). The ikaite-to-vaterite transformation: New evidence from diffraction and imaging. *Journal of Applied Crystallography*, 42(2), 225–233. <https://doi.org/10.1107/S0021889809005810>
- Tegner, C., Storey, M., Holm, P. M., Thorarinsson, S. B., Zhao, X., Lo, C., & Knudsen, M. F. (2011). Magmatism and Eureka deformation in the High Arctic Large Igneous Province: Ar – 39 Ar age of Kap Washington Group volcanics, North Greenland. *Earth and Planetary Science Letters*, 303(3–4), 203–214. <https://doi.org/10.1016/j.epsl.2010.12.047>
- Teichert, B. M. A., & Luppold, F. W. (2013). Glendonites from an Early Jurassic methane seep — Climate or methane indicators? *Palaeogeography, Palaeoclimatology, Palaeoecology*, 390, 81–93. <https://doi.org/10.1016/j.palaeo.2013.03.001>
- Tissot, B.P., and Welte, D.H. (1978) Coal and its Relation to Oil and Gas. In: Petroleum Formation and Occurrence. Springer, Berlin, Heidelberg. https://doi.org/10.1007/978-3-642-96446-6_12
- Toboła, T., & Botor, D. (2020). Raman spectroscopy of organic matter and rare minerals in the Kłodawa Salt Dome (Central Poland) cap-rock and Triassic cover – Indicators of hydrothermal solution migration. *Spectrochimica Acta - Part A: Molecular and Biomolecular Spectroscopy*, 231. <https://doi.org/10.1016/j.saa.2020.118121>
- Tollefsen, E., Stockmann, G., Skelton, A., Mörth, C.-M., Dupraz, C., & Sturkell, E. (2018). Chemical controls on ikaite formation. *Mineralogical Magazine*, 82(5), 1119–1129. <https://doi.org/10.1180/mgm.2018.110>
- Tollefsen, E., Balic-Zunic, T., Mörth, C. M., Brüchert, V., Lee, C. C., & Skelton, A. (2020). Ikaite nucleation at 35 °C challenges the use of glendonite as a paleotemperature indicator. *Scientific Reports*, 10(1), 1–10. <https://doi.org/10.1038/s41598-020-64751-5>
- Tzachristas, A., Natsi, P. D., Kanellopoulou, D. G., Parthenios, J., Koutsoukos, P. G., Paraskeva, C. A., & Sygouni, V. (2021). Mineral Scaling in the Presence of Oil-Water Interfaces Combined with the Substrate's Wettability Effect: From Batch to Microfluidic Experiments. *Industrial and Engineering Chemistry Research*, 60(22), 8244–8254. <https://doi.org/10.1021/acs.iecr.1c00804>
- Vickers, M., Watkinson, M., Price, G. D., & Jerrett, R. (2018). An improved model for the ikaite-glendonite transformation: Evidence from the lower cretaceous of spitsbergen, Svalbard. *Norsk Geologisk Tidsskrift*, 98(1), 1–15. <https://doi.org/10.17850/njg98-1-01>
- Vickers, M. L., Lengger, S. K., Bernasconi, S. M., Thibault, N., Schultz, B. P., Fernandez, A., Ullmann, C. V., McCormack, P., Bjerrum, C. J., Rasmussen, J. A., Hougård, I. W., & Korte, C. (2020). Cold spells in the Nordic Seas during the early Eocene Greenhouse. *Nature Communications*, 11(1), 1–12. <https://doi.org/10.1038/s41467-020-18558-7>
- Wehrmeister, U., Soldati, A. L., Jacob, D. E., Häger, T., & Hofmeister, W. (2010). Raman spectroscopy of synthetic, geological and biological vaterite: A Raman spectroscopic study. *Journal of Raman Spectroscopy*, 41(2), 193–201. <https://doi.org/10.1002/jrs.2438>
- Whiticar, M. J. (1999). Carbon and hydrogen isotope systematics of bacterial formation and oxidation of methane. *Chemical Geology*, 161(1), 291–314. [https://doi.org/10.1016/S0009-2541\(99\)00092-3](https://doi.org/10.1016/S0009-2541(99)00092-3)
- Wolverson, D. (2008). Raman spectroscopy. In *Characterization of Semiconductor Heterostructures and Nanostructures*. <https://doi.org/10.1016/B978-0-444-53099-8.00008-7>

Zabel, M., & Schulz, H. D. (2001). Importance of submarine landslides for non-steady state conditions in pore water systems - Lower Zaire (Congo) deep-sea fan. *Marine Geology*, 176(1–4), 87–99. [https://doi.org/10.1016/S0025-3227\(01\)00164-5](https://doi.org/10.1016/S0025-3227(01)00164-5)

Zhang, Z., Gao, Y., Meldrum, F. C., Shui, L., Wang, Z., Li, S., & Li, G. (2020). Investigating the Nucleation Kinetics of Calcium Carbonate Using a Zero-Water-Loss Microfluidic Chip. *Crystal Growth and Design*, 20(4), 2787–2795. <https://doi.org/10.1021/acs.cgd.0c00191>

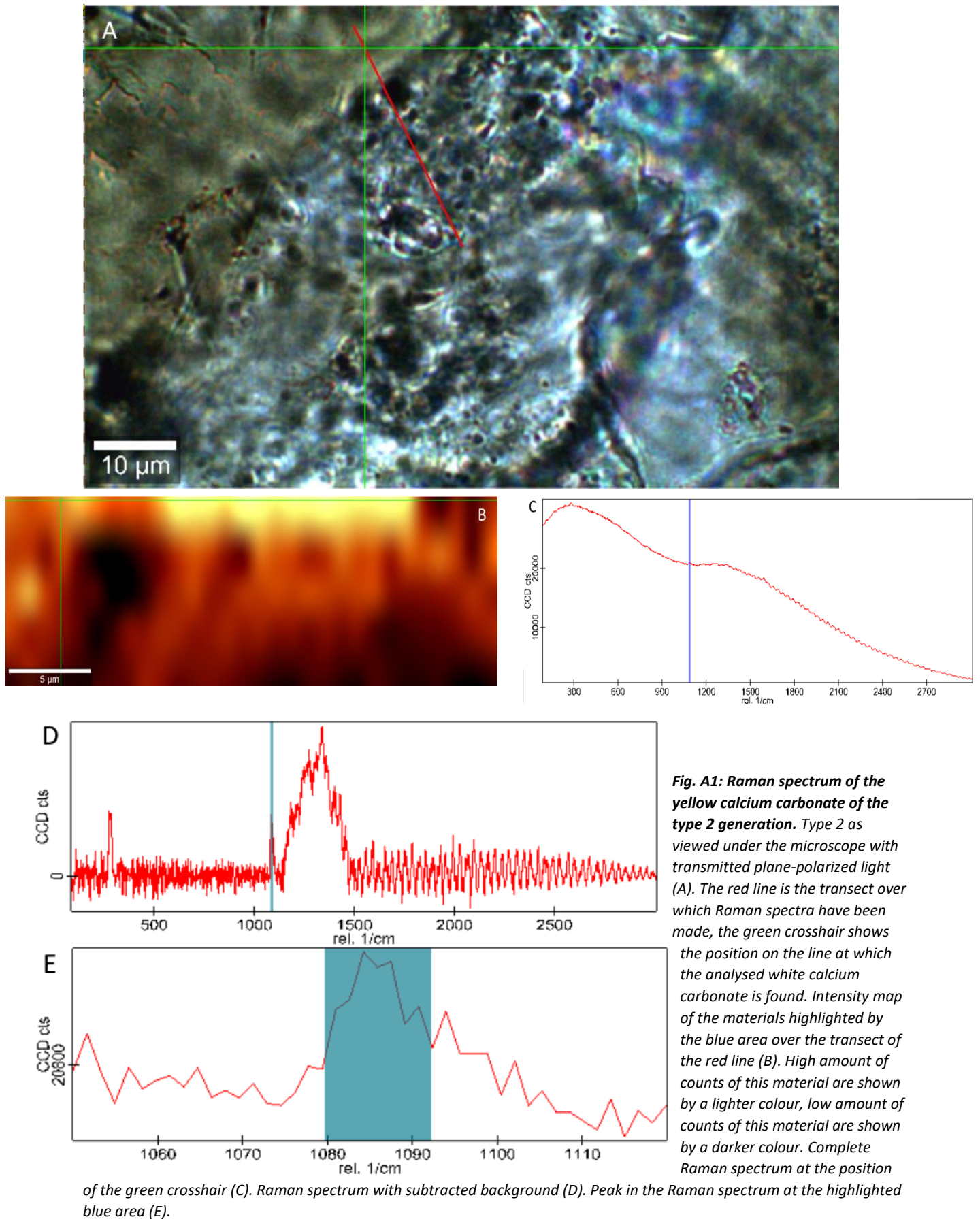
Acknowledgements

I am grateful to Bas van de Schootbrugge for providing me a chance to work on this project and supervising me on it. I thank Helge Niemann, Stefan Schouten, and Francien Peterse for directing me to this project. I am also grateful to Helen King for being my 2nd supervisor and for the help with Raman spectroscopy.

I want to thank Francien Peterse and specifically Klaas Nierop for all their help during the biomarker analysis. I am thankful to Leonard Bik for making the thin sections for this study.

I am thankful to Madeleine Vickers with whom I had fruitful discussions.

Appendix



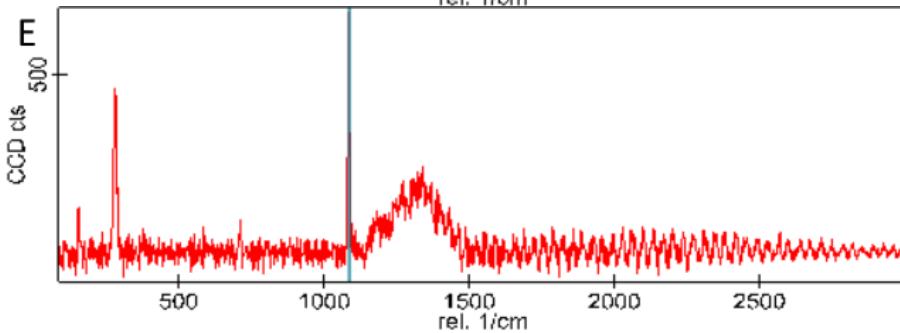
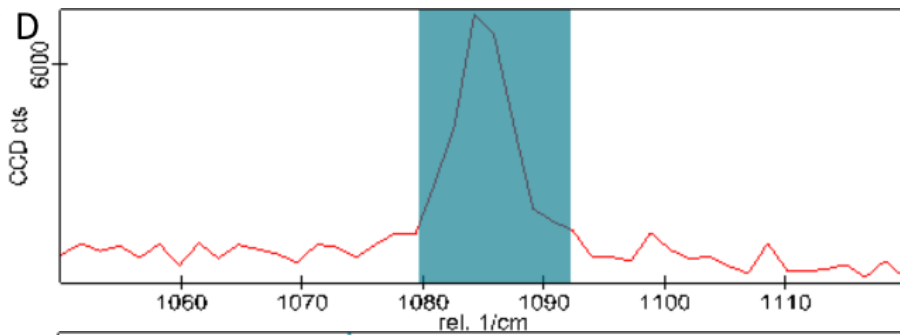
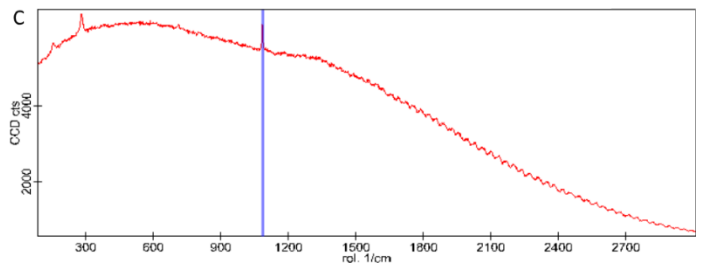
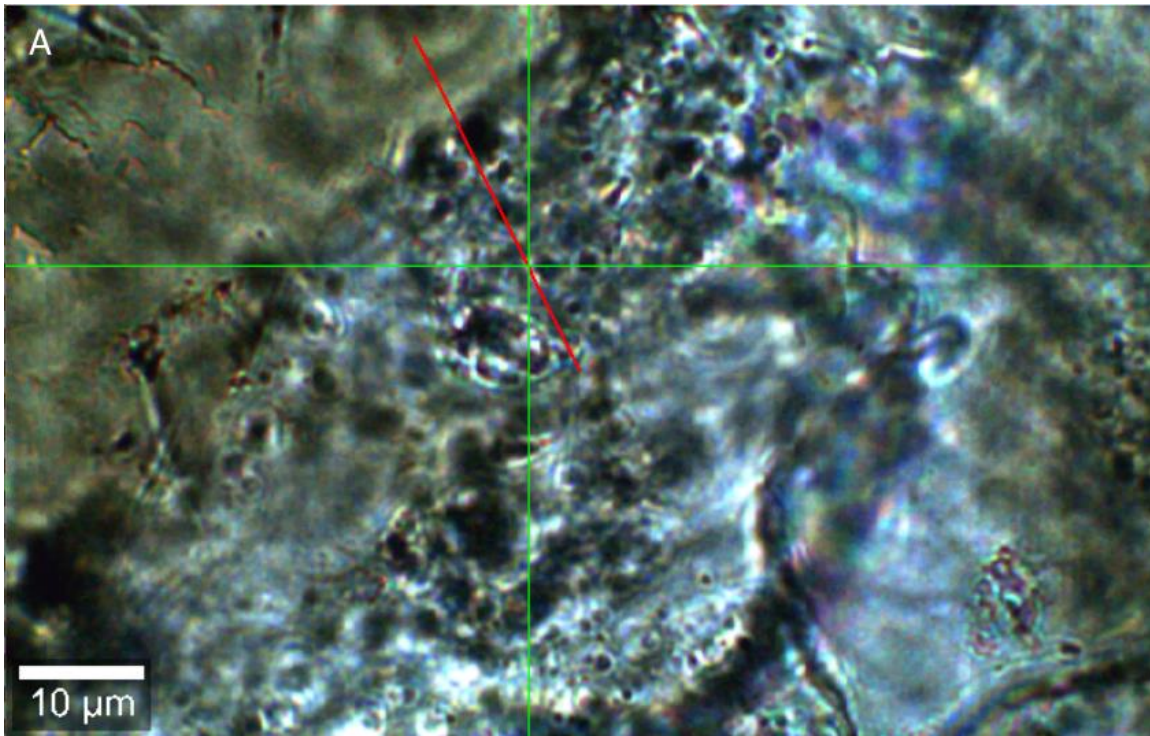


Fig. A2: Raman spectrum of the white calcium carbonate of the type 1b generation. Type 1b as viewed under the microscope with transmitted plane-polarized light (A). The red line is the transect over which Raman spectra have been made, the green crosshair shows the position on the line at which the analysed white calcium carbonate is found. Intensity map of the materials highlighted by the blue area over the transect of the red line (B). High amount of counts of this material are shown by a lighter colour, low amount of counts of this material are shown by a darker colour. Complete Raman spectrum at the position of the green crosshair (C). Raman spectrum with subtracted background (D). Peak in the Raman spectrum at the highlighted blue area (E).

Appendix B

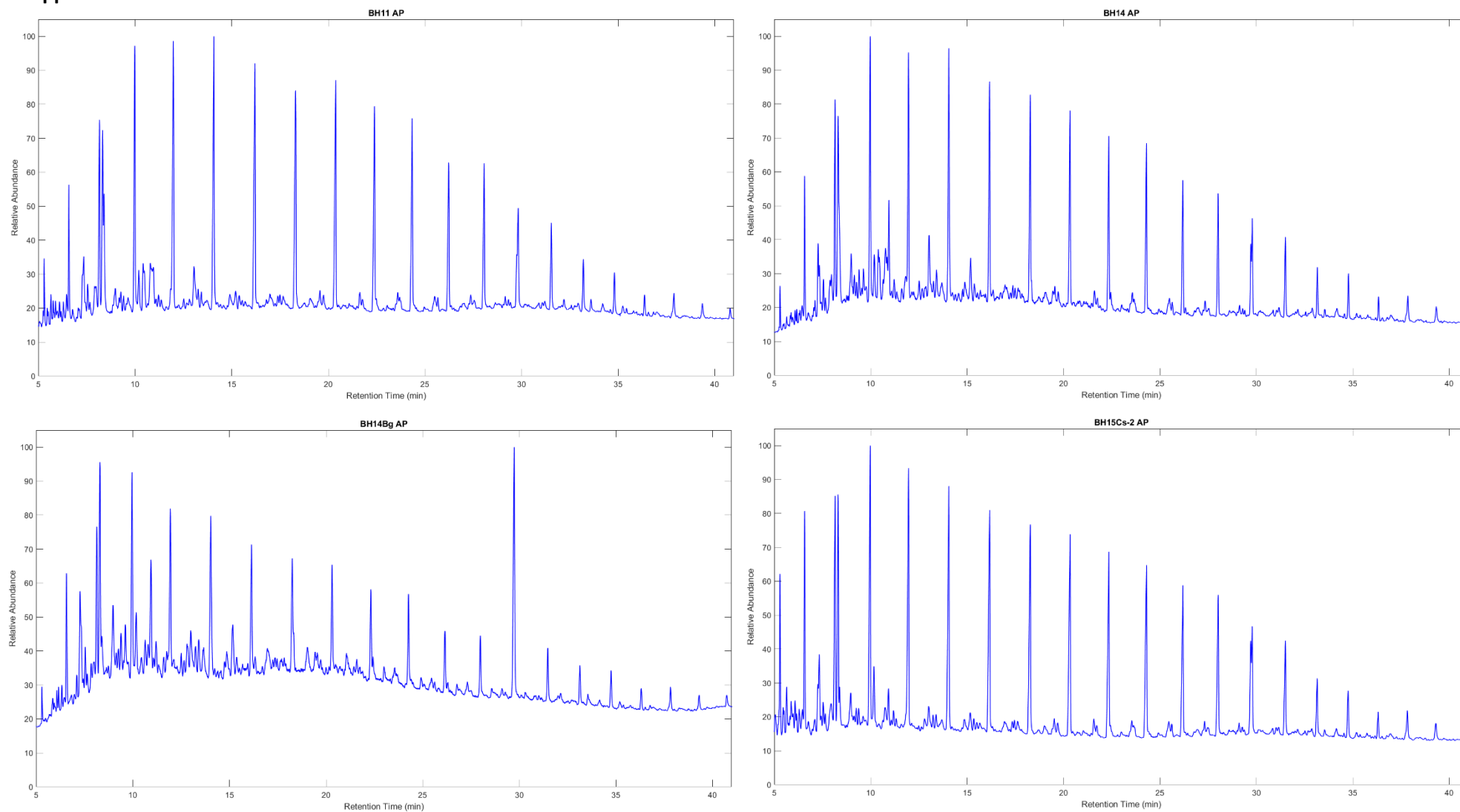


Fig. B1: Gas chromatograms of the apolar fraction of glendonite and sediment samples. BH14Bg AP is a glendonite sample while the rest are sediment samples.

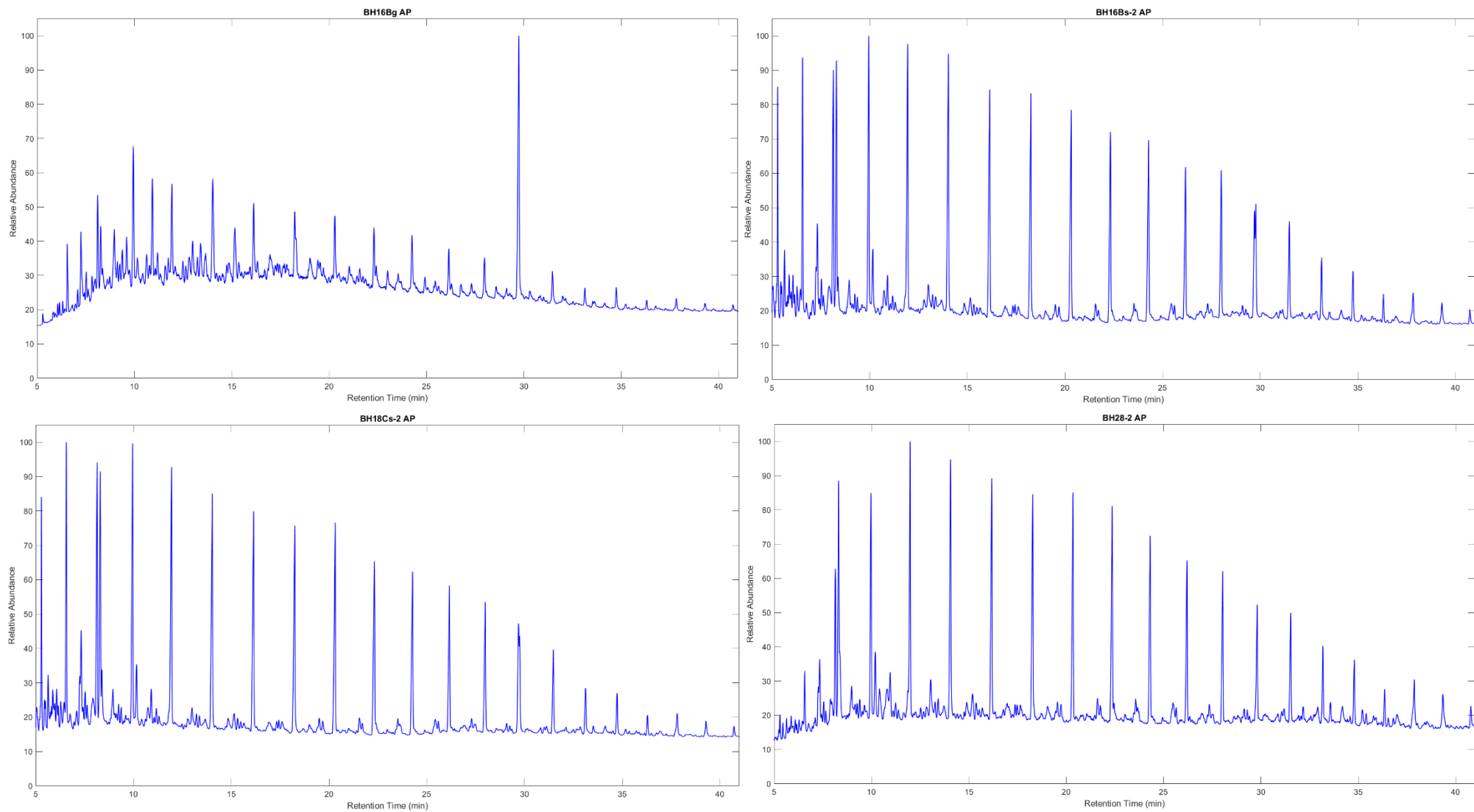


Fig. B2: Gas chromatograms of the apolar fraction of glendonite and sediment samples. BH16Bg AP is a glendonite sample while the rest are sediment samples.